GEOPHYSICAL INVESTIGATIONS AND INTERACTIVE VISUALIZATIONS OF

THE CHARLIE-GIBBS FRACTURE ZONE

By

ISLA TURCKE

A Thesis

Submitted to the School of Interdisciplinary Science

In Partial Fulfilment of the Requirements

For the Degree

Bachelor of
Science

McMaster University

BACHELOR OF SCIENCE (2022)　　　　　　McMaster University

School of Interdisciplinary Science　　　　　Hamilton, Ontario

TITLE: Geophysical Investigations and Interactive Visualizations of the Charlie-Gibbs Fracture Zone

AUTHOR: Isla Turcke

SUPERVISOR: Dr. Alexander Peace

NUMBER OF PAGES: 36

Abstract

Oceanic transform faults and their associated fracture zones are key constituents of tectonic processes and regions of high seismic activity. While they are of scientific interest, the remote nature and extreme ocean depths at these sites limits manual exploration and sample collection. This challenge has promoted the use of other methods of data collection and analysis such as satellite altimetry, ship depth-soundings, and computational modelling. Despite decades of study and large quantities of data, these features remain poorly understood. A common difficulty in analyzing these structures lies in the fact that many geophysical datasets are largely disjointed and often have incompatible resolutions and file formats. Additionally, some datasets must be derived from others or require processing in order to discern features of interest.

This thesis aims to broaden our understanding of the Charlie-Gibbs Fracture Zone, an extensive structure found in the North-Atlantic Ocean. As the largest interruption of the Mid-Atlantic Ridge between Iceland and the Azores, this unique system of two parallel FZs is of particular interest to many geoscientists. Through the processing and compilation of several geophysical datasets, this study sought to find computational methods that could highlight key structural features, enhance small-scall anomalies, and allow hidden patterns to be seen.

Freely available datasets for bathymetry, free-air gravity anomaly, and magnetic anomaly were downloaded and read into GMT (the general mapping tools), where they were converted to grid files and clipped to the study region. A bathymetric illumination grid was calculated using the directional derivative of the bathymetry grid, and the Bouguer anomaly was derived from the bathymetry and free-air gravity anomaly grids. Upward continuation and wavelength filtering were applied to both the free-air gravity anomaly and magnetic anomaly datasets, to compare the effects of the different processes and enhance small-scale anomalies and linear features. Transects across final datasets were sampled and intermediate values were interpolated to create profiles in Microsoft Excel. All resulting datasets were converted to netCDF files, from which raster layers were produced in ArcGIS Pro. This allowed the findings to be presented in a new and educational way: through the creation of an online interactive story map.

Acknowledgements

I would like to thank the following people for their contributions to this thesis:

Firstly, my supervisor, Dr. Alexander Peace, for his guidance and expertise throughout this project. The many wonderful professors that I have had, for developing both my mind and my interests. My partner, Jonathan Spence, for giving me the idea to make a story map. Professor Pat DeLuca and my peer and friend Joshua Riswick, for helping me navigate the world of ArcGIS Online. Lastly, I would like to thank my peers in the Integrated Science program as well as my friends and family, for supporting me throughout this undergraduate adventure.

Table of Contents

Introduction

Region of Interest

This study works on the North-Atlantic Ocean, focusing on the area around the Charlie-Gibbs Fracture Zone (CGFZ). The CGFZ is a set of two parallel transform faults (TFs) found along the Mid-Atlantic Ridge (MAR), a mid-ocean ridge (MOR) that runs the length of the Atlantic Ocean. Surrounding this pair of transform faults is an extensive fracture zone (FZ). These structural components of the CGFZ will be discussed shortly.

The exact region most thoroughly examined falls between 50° and 60° North of the equator, and between 50° and 20° West of the prime meridian. That having been said, the data sets were initially mapped over a larger region to validate that the data sets were appearing as expected and being mapped properly onto the globe. The benefit of using a larger area for this purpose was that the edges of the continental shelves of North America, Greenland, and Europe were included in the region. These continental areas were used to help assess the validity of the data sets through their well-known locations and known differences in their geophysical properties compared to oceanic areas. For example, we expect elevation to be above sea level over continents and below sea level over the ocean. By mapping an elevation dataset along with outlines of the world's continents, one could assess whether this expectation was being met.
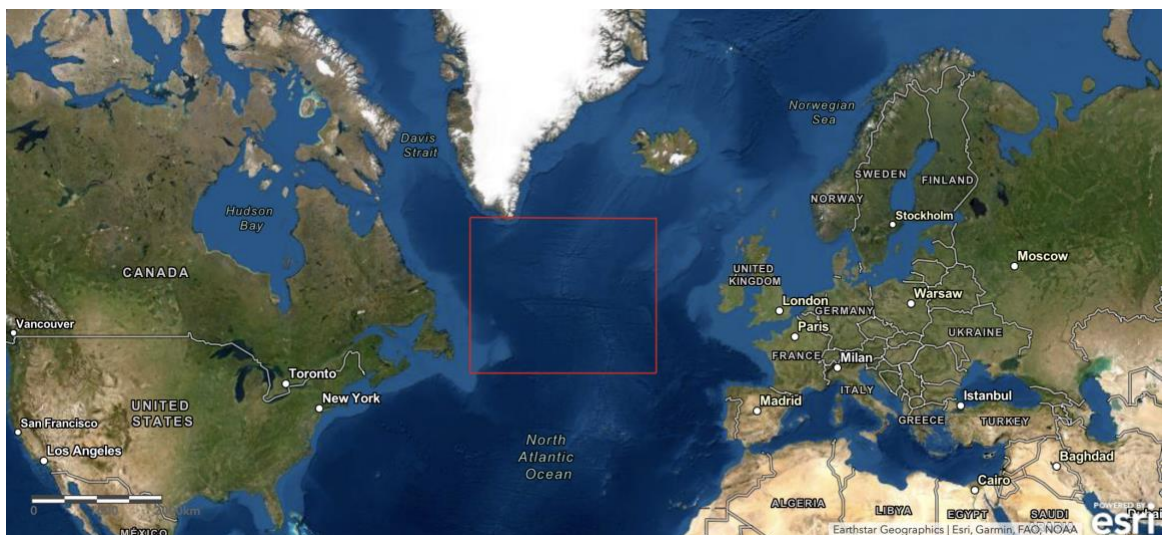
Figure 1: North-Atlantic Ocean with study area contained within the red rectangle.

Geological Background

Plate Tectonics

The plate tectonics model was built upon the concept of continental drift, which was first proposed by Abraham Ortelius in 1596 and then independently and more fully developed by Alfred Wegener in 1912 (Hallam, 1975). While initially ridiculed, this idea was instrumental in getting to where we are today; and the success of plate tectonics led to a comprehensive reinterpretation of Earth's large-scale history (Molnar, 1988).

Earth's lithosphere, which is made up of continental or oceanic crust and upper-most mantle, is broken up into large and relatively rigid slabs called tectonic plates. The thickness of each plate depends greatly on the type of crust that tops it, as continental crust averages 40 km in thickness while oceanic crust averages only 6 km (Coltice et al., n.d.). Plate tectonics is the widely accepted theory that describes the motion of these plates atop the asthenosphere, which is the much denser and more ductile layer beneath the lithosphere. The asthenosphere lies between approximately 100 km and 410 km below Earth's surface, and while temperatures at these depths are more than high enough to melt rock on the surface, the intense pressure keeps the rocks only semi-molten (Poldervaart, 1955). Descending from the asthenosphere further into the mantle, both pressure and temperature increase, with a geothermal gradient of about 25 K km^{-1} of depth. In the most malleable part of the mantle, convection currents are postulated to drive tectonic activity due to the induced flow of hotter material rising from closer to the core and cooler material sinking from closer to the surface (Bercovici, 2011). The rising and sinking of material interacts most strongly with Earth's surface at hot spots, volcanoes, and along plate boundaries (Molnar, 1988).

Plate Boundaries

Since the plates are moving in different directions and at different rates – typically between two and twenty centimeters per year – the boundaries between plates are geologically very active (Coltice et al., n.d.). There are three main types of plate boundary as shown in Figure 2: divergent, where two plates pull away from each other; convergent, where one plate subducts under the other; and transform, where plates slide horizontally past one another (Anon., 2021b). The primary region of interest is found along a divergent boundary, so this will be our focus.
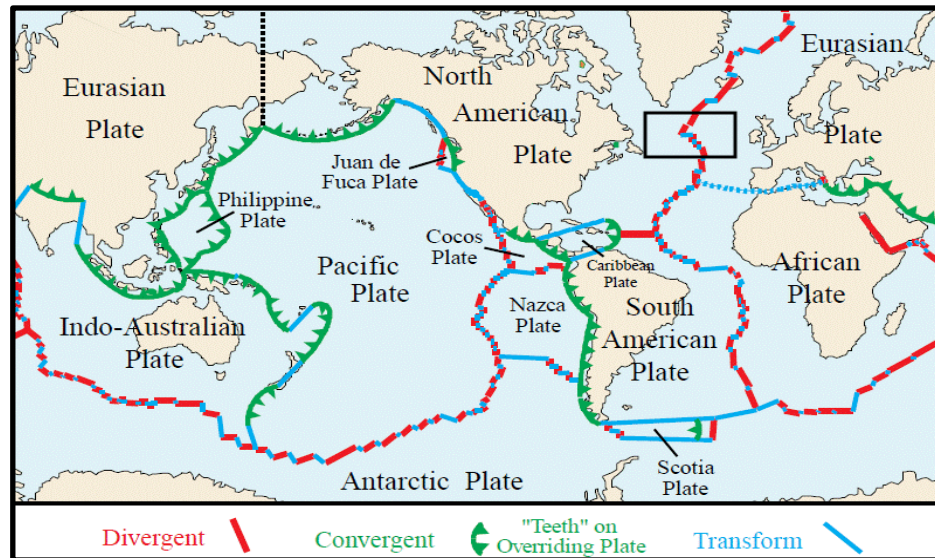
Figure 2: Plate boundary types; study region in black rectangle (Pitman and von Huene, 2020).

As two plates pull apart, there is an upwelling of hotter material from the upper mantle. This creates topographically high regions along the boundary as the mantle pushes up the oceanic crust that has become thinner, warmer, and less dense (Pitman and von Huene, 2020). These elevated regions are called mid-ocean ridges (MORs). Possibly the most well-known MOR is the Mid-Atlantic Ridge (MAR), which extends from the waters North-East of Greenland to South-West of the southern tip of Africa (Anon., 2021a). Comparing Figure 2 above with Figure 3 below, we can see how the major MORs all occur along divergent plate boundaries.
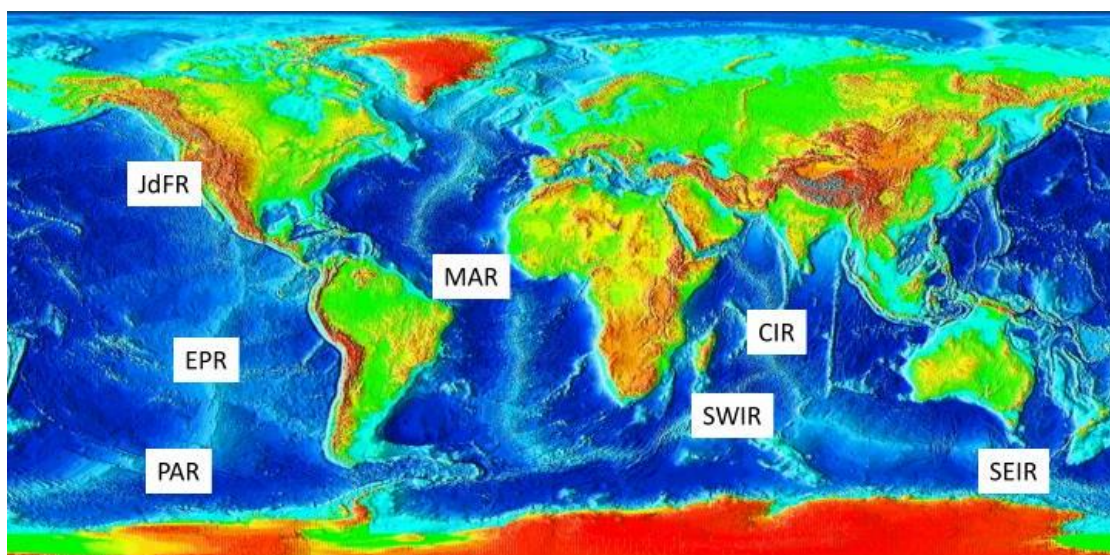
Figure 3: Major MORs, with the MOR of interest being the Mid-Atlantic Ridge (MAR).

Mid-Ocean Ridges, Transform Faults, and Fracture Zones

Mid-ocean ridges are often characterized as submarine mountain ranges, where basaltic magma from the mantle forms new oceanic crust in the rift valley along the spreading axis (Vogt, 2019). The slopes outside the MOR are shallow, due to the combined effects of continued seafloor spreading and thermal subsidence (Bercovici, 2011). Since the plates do not have perfectly defined straight edges, divergent boundaries are comprised of many spreading centers offset by discontinuities, most in the form of transform faults (Kearey, Klepeis and Vine, 2009).

Transform faults (TFs) accommodate the divergence of plates between adjacent segments of MORs (Anon., 2021b). The crust on either side of a TF belongs to different plates, and thus the direction of plate motion across the TF is opposing. This opposing motion of the two plates generates immense amounts of friction as the two plates struggle to move past one another (Kearey, Klepeis and Vine, 2009). This leads to TFs being regions of high tectonic activity, which can generate enormous and devastating earthquakes due to the shallow nature of the foci (Earle, 2015).

Extending for up to thousands of kilometers on either side of these active boundaries are fracture zones (FZ), which correspond to intra-plate junctions between crustal regions of different ages (Hensen et al., 2019). In each FZs, all the crust belongs to the same plate and hence the direction of plate motion is the same throughout each FZ. While it was once thought that FZs were tectonically inactive, it has now been shown that several FZs are seismically active and can also produce earthquakes of large magnitudes such as the 2012 Sumatra-Wharton Basin earthquake (Hensen et al., 2019).
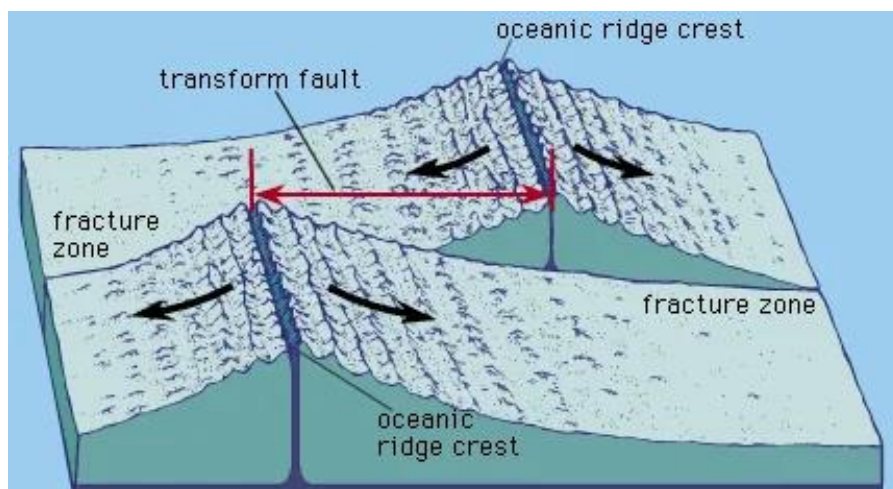
Figure 4: Two segments of an MOR offset by a transform fault, with fracture zones extending on either side. Arrows depict direction of plate motion (Encyclopedia Britanica, Inc., 1994).

Project Rational

  As technology advances and we further explore the earth, geophysical datasets are continuously being updated and added to, providing many improvements in areas such as coverage (proportion of Earth where measurements have been taken), resolution (spatial frequency with which measurements are taken), and accuracy (how close the measured values are to the true values). It is important that these updated datasets are then analyzed and interpreted, in order to correspondingly update our understanding of these features. Such work can provide insights regarding the structural geology of the region, and it allows for the creation of new predictive models of both historical and future tectonic processes.

  This thesis aims to examine several geophysical properties of the Charlie-Gibbs Fracture Zone. As a region of high seismic activity, which can trigger earthquakes and drive volcanic activity, increasing our understanding of features such as this one is of particular interest to geoscientists (Keen, Dafoe and Dickie, 2014). Three geophysical properties were chosen to investigate: bathymetry, gravity anomaly, and magnetic anomaly. Bathymetry gives us a picture of the physical structure of the seafloor and provides ocean depth values as well. This is critical for aligning the anomaly data to the structural features on the ocean floor. Gravity anomaly data was chosen for its relationship with density, as it can be interpreted to make predictions about the composition and structure of materials below the surface (Cochran and Talwani, 1978). Magnetic anomaly data can also provide insight into the subsurface of the earth's crust. In oceanic crust, magnetic anomalies can reveal the evolution of the crust over time. Potential field anomaly data sets are commonly used in resource exploration and other geological fields (Meyer, Chulliat and Saltus, 2017). Thus, it is useful to develop the skills needed to handle, process, and analyze these data sets.

  Unfortunately, the analysis and interpretation of these data sets can be hindered by the fact that many geophysical data sets are largely disjointed. Data sets are collected via different methods, cover differing areas, and often have incompatible resolutions and file formats. Additionally, some data sets must be derived from others or require processing to reveal patterns or to discern features of interest. This makes it difficult for members of the public to access, view, and understand these data sets, let alone the observations and results that can be drawn from them. To address this challenge, all data sets acquired and produced during this study will be visually presented and discussed in an online, interactive story map.

Geological Setting

The Opening of the North-Atlantic Ocean

In the first stage of Pangea's breakup, rifting between Laurentia and Africa led to the divergence of the two plates and the beginning of the formation of the north-central Atlantic Ocean (Hallam, 1971). During the second major phase, the South-Atlantic opened as South America drifted westward away from Africa. Greenland separating from Eurasia during the final stages of Pangea's breakup initiated the expansion of the vast North-Atlantic ocean that exists today (Pe-Piper et al., 2007). This process is illustrated below using snapshots from a plate reconstruction model by Muller et al..
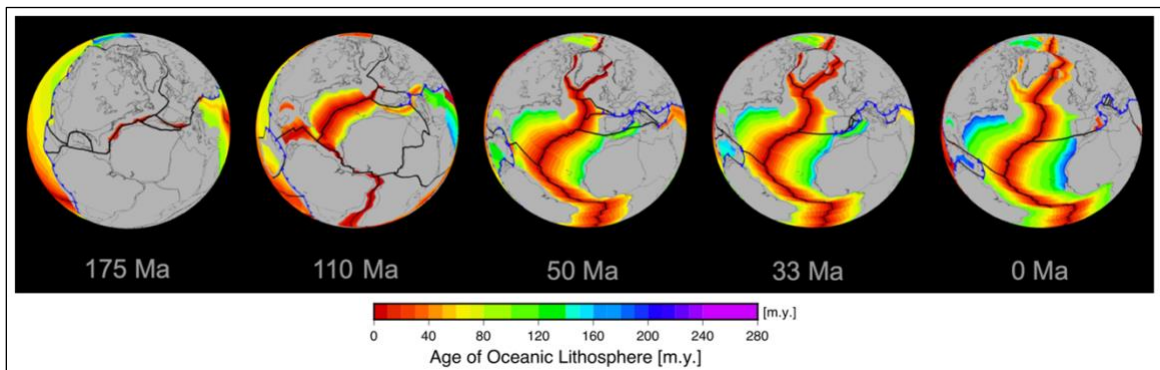
Figure 5: Snapshots in time of the opening of the Atlantic Ocean (Muller et al., 2019).

With new crust being generated along these divergent boundaries and older crust spreading with the plates, the above figure illustrates the development of the great MAR. The CGFZ, which is evident in the snapshot at 0 Ma, can also be traced back all the way to roughly 50 Ma. This divergence continues today, with an average spreading rate of 2.5 cm yr^{-1}, equivalent to 25 km per million years (Anon., 2021b).

Structure of the Charlie-Gibbs Fracture Zone.

The Charlie-Gibbs fracture zone (CGFZ) is the most prominent discontinuity along the MAR. It's extensive FZ can be traced for over two-thousand kilometers W-E across the North-Atlantic, stretching from North-East of Newfoundland, Canada towards the southern tip of Ireland (White and Williams, 1986). The CGFZ is a system of two parallel right-lateral TFs, each with their own FZ. The total offset between the northern MAR segment coming from Iceland and the southern MAR segment stretching towards the Azores Triple Junction is 350 km to the east. The northern TF provides 230 km of eastern offset and the southern TF provides the other 120 km (Skolotnev et al., 2021b).

These two transform valleys are separated by an intra-transform ridge, which is cut at 31.8°W by an intra-transform spreading centre approximately 40 km N-S. A unique feature of the CGFZ is that the MAR segments to its north and south are very different in morphology and thus potentially in formation (Skolotnev et al., 2021a).

Contrasting the shallow sloping sides of MOR structures, marine transform fault and fracture zone systems have a characteristic morphology of steep and narrow valleys that cut deep into the lithosphere (Sæl et al., 2021). Given the presence of the CGFZ on the MAR, more complex bathymetric profiles are expected in this region. The large-scale structure of the CGFZ and adjacent segments of the MAR can be seen in the figure below.
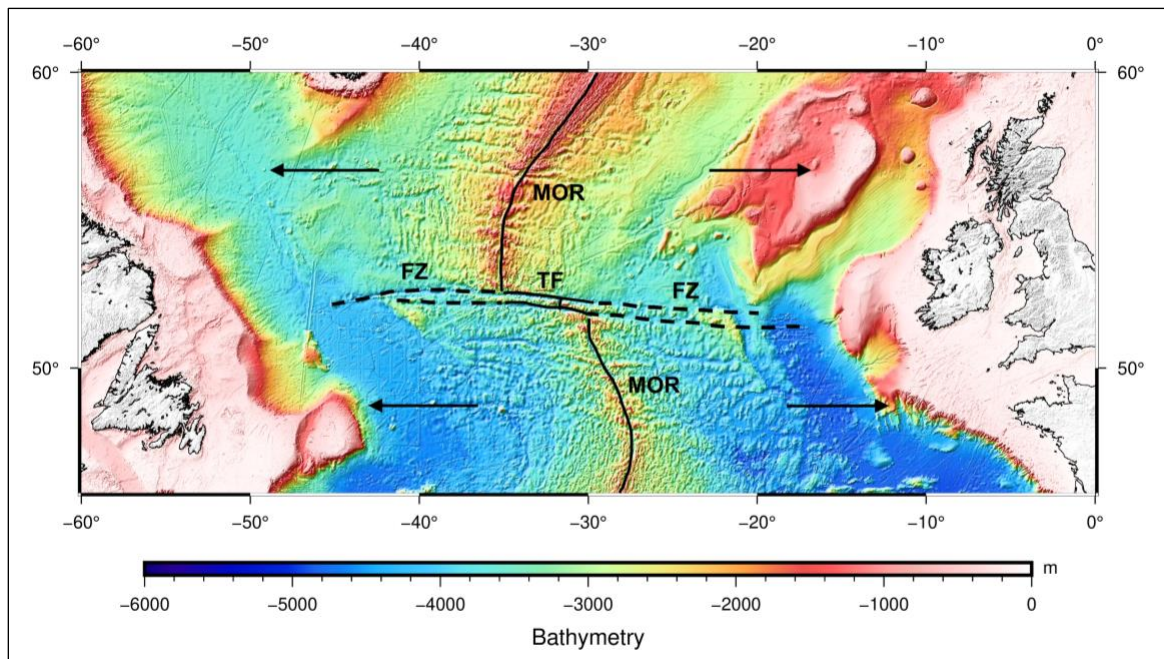
Figure 6: Bathymetric map of the North-Atlantic Ocean, showing the full-extent of the CGFZ. Annotated features: Mid-Ocean Ridge (MOR), the transform faults (TF) and fracture zones (FZ). Arrows show direction of plate movement. (Produced by author with data from (Smith and Sandwell, 1997).)

Methods

Data Sets

Three data sets were used in this study: an image file containing global seafloor topography (bathymetry) values, an image file of global free-air gravity anomaly (FAGA), and a comma separated values file of global magnetic anomaly (MA). See Table 1 below for information on the three data sets used.

Table 1: Information on data sets used and list of data sets produced.

Geophysical Property:	Data set Name:	Resolution and File Type:	Source Website and Reference:
Bathymetry	topo_19.1	1 arc-min .img	Scripps Institution of Oceanography (Sandwell and Smith, 1997)
Free-Air Gravity Anomaly	grav_31.1	1 arc-min .img	Scripps Institution of Oceanography (Sandwell et al., 2014)
Magnetic Anomaly	EMAG2v3	2 arc-min .csv	NOAA – National Centres for Environnemental Information (Meyer, Chulliat and Saltus, 2017)

Bathymetry Data

Bathymetry is the term for seafloor topography, which is elevation when the surface of Earth's crust is below sea level. Bathymetry values can be estimated from marine gravity anomalies, which allows for seafloor topography to be mapped even in poorly surveyed regions. *Sandwell and Smith* combined satellite altimeter-derived gravity data from Geosat and ERS-1 with the most comprehensive assemblage of ship-depth soundings to produce a global, high-resolution bathymetric map.

Free-Air Gravity Anomaly Data

A recent global marine gravity model, presented by Sandwell et al. in 2014, combines previously existing data with new radar altimeter measurements from Cryo-Sat-2, Envisat, and Jason-1 satellites. This new model has an accuracy of about 2 mGal, making it roughly twice as accurate as previous models, as well as significantly improved resolution and noise reduction. In 2010, CryoSat-2 was launched into a 369-day orbit

where the ground tracks were permitted to drift within 5 km bands, providing dense track coverage (track spacing 2.5 km). In the same year, Envisat was moved from its 35-day exact repeat orbit into a drifting track, where it collected data for 18 months before its demise. Jason-1 was launched into a 406-day orbit in 2012, providing fourteen months of dense track coverage (track spacing of 7.5 km at the equator) during its geodetic phase.

These missions' datasets augment older altimeter data from Envisat, Geosat, and ERS-1. Both the precision and accuracy of gravity data rely on dense track spacing; thus, the longer period orbits of CryoSat-2 and Jason-1 were favourable. Envisat provided dense track coverage at high latitudes by combining data collected during its drifting track phase with ten years of data collected along its exact repeat track. Marine data was collected by each of these altimeters at a pulse repetition frequency (PRF) of around 2 kHz. This is roughly twice the PRF of earlier satellite altimeters and is thought to maximize the frequency of statistically independent measurements. The improved range precision and dense coverage from CryoSat-2, Envisat and Jason-1 is thought to have led to a significant increase in the accuracy of the data set (Sandwell et al., 2014).

A correction known as the free-air correction had already been applied to the data set, to account for the effects of measurements taken at differing elevations. This correction brings all measurement points down to sea level. All measurements must be corrected to the same level (sea level in this case), since the strength of the gravitational field depends on the radius from the centre of the earth to the measurement elevation(Hackney and Featherstone, 2003).

Magnetic Anomaly Data

Magnetic anomaly data was accessed from the third version of the Earth Magnetic Anomaly Grid at 2 arc minute resolution (EMAG2v3). This dataset maps the location, intensity, and extent of lithospheric magnetic anomalies, providing full global coverage from -90°S to 90°N and 0°E to 360°E. The previous version, EMAG2, has been widely used for resource exploration, plate reconstructions, and studies looking at various geological environments including fault zones, continental margins, and MORs. Unlike EMAG2, no a priori information was used to fill data gaps or otherwise influence version 3. EMAG2v3 includes an additional 50 million data points, mostly over marine areas, making it a great resource for the scope of this project. The full database covers 10.5 million track-line miles and consists of 3,255 surveys and 76.1 million data points.

The methods of data collection include satellite data, magnetic observatory data, and marine and airborne track-line surveys. The National Centers for Environmental Information (NCEI) compiled these surveys over the last five decades from over 100 institutions. Keeping the future in mind, this dataset was designed to allow for easy and frequent updates as more data is becomes available.

With improvements to data preprocessing methods, several outliers in marine and airborne track-line data were eliminated. Points with a total calculated anomaly of >1,000 nT and any subsequent points with a gradient of over 100 nT/km were discarded as noise. Long-wavelength anomalies (>300 km) were replaced by the newer and higher resolution MF7 satellite-based lithospheric field model, and oceanic areas were subdivided into 21 tiles for error estimation. Each tile overlaps adjacent tiles by 1° and airborne data were extended 5° past tile boundaries to smooth the transitions between tiles and avoid edge effects. The data were gridded using a Kriging method, due to its ability to handle data with high density and line azimuth variability. Airborne data was used to fill gaps when continental or marine datasets were not already sufficiently covered. Assuming an average measurement altitude of 4 km, the airborne data were downward continued to sea level. For a more thorough explanation of the preprocessing that was applied to this data set, please see (Meyer, Chulliat and Saltus, 2017).

Software and Processing Overview

The Generic Mapping Tools version 6 (GMT) (Wessel et al., 2019) software was the primary software used for this project. The acquired data sets were downloaded from their respective websites (see Table 1) and read into GMT. This software was used for all the processing that was applied to the data sets, as well as for clipping the data sets to the desired study region. This processing includes taking directional derivatives, calculating the Bouguer anomaly, upward continuation, grid math, filling holes in data sets, reduction to the pole of magnetic anomaly data, and application of high-pass, low-pass, and band-pass filters. GMT was also used to plot all the data sets, both for quality control and exploration of the initial data sets, as well as for visualization and comparison of data sets after various processing had been applied. Lastly, GMT allowed for transects across several data sets to be sampled, interpolating intermediate values, and outputting a new csv file. This output transect data was imported into Microsoft Excel and vertical profile graphs were created. See Table 2 below for a summary of which GMT functions were used to produce each novel data set.

Table 2: Overview of data set processing in GMT.

Source Data:	Function(s):	Data set(s) Produced (Clipped to CGFZ region):
Bathymetry	• img2grd	• Bathymetry
	• img2grd • grdgradient	• Directional derivative of bathymetry from the NW
Free-air gravity anomaly	• img2grd	• Free-air anomaly (FAA)
	• img2grd • gravfft • grdmath (SUB)	• Bouguer anomaly (requires bathymetry data as well)
	• img2grd • grdfft	• FAA upward continued 10 km • FAA upward continued 20 km
	• img2grd • grdfft • grdmath (SUB)	• FAA minus FAA upward continued 10 km • FAA minus FAA upward continued 20 km
	• img2grd • grdfft	• FAA with high-pass filter • FAA with low-pass filter • FAA with band-pass filter
	• img2grd • grdfft • grdgradient	• N-S directional derivative of high-pass filtered FAA • E-W directional derivative of high-pass filtered FAA • N-S directional derivative of low-pass filtered FAA • E-W directional derivative of low-pass filtered FAA • N-S directional derivative of band-pass filtered FAA • E-W directional derivative of band-pass filtered FAA
Magnetic anomaly	• xyz2grd	• Magnetic anomaly
	• xyz2grd • grdfill • grdredpol	• Magnetic anomaly – holes filled and reduction to the pole applied (MA-RTP)
	• xyz2grd • grdfft	• MA-RTP upward continued 10 km • MA-RTP upward continued 20 km
	• xyz2grd • grdfft • grdmath (SUB)	• MA-RTP minus MA-RTP upward continued 10 km • MA-RTP minus MA-RTP upward continued 20 km
	• xyz2grd • grdfft •	• MA-RTP with high-pass filter • MA-RTP with low-pass filter • MA-RTP with band-pass filter
	• xyz2grd • grdfft • grdgradient	• N-S directional derivative of high-pass filtered MA-RTP • E-W directional derivative of high-pass filtered MA-RTP • N-S directional derivative of low-pass filtered MA-RTP • E-W directional derivative of low-pass filtered MA-RTP • N-S directional derivative of band-pass filtered MA-RTP • E-W directional derivative of band-pass filtered MA-RTP

The final software used for this project was ArcGIS Pro, a powerful GIS application from ESRI that is known for data visualization and advance analysis (ESRI, 2022d). The principal reason for the use of this software was the ability to publish raster layers as tile layers to ArcGIS Online, which is an ESRI-administered cloud infrastructure. In ArcGIS Pro, all data sets from Table 2 above were made into raster layers, which were then converted to tile layers and published to ArcGIS online. From there, an interactive story map was made, using the many tile layers as well as the vertical profiles.

Data Visualization and Validation

Before beginning any processing on the acquired data sets, the initial data sets were read into GMT, converted to grid files (.grd), and plotted. This allowed for these large data sets to be visually explored and for some quality control to be done. The plots were made over several regions in order to compare to data sets plotted by other geoscientists and ensure that the data had been downloaded, read, and mapped correctly. A cylindrical Mercator projection was used for all plots. The grid files were later converted to netCDF files (.nc) to allow them to be imported into ArcGIS Pro and made into raster layers. The conversion process using GMT is outlined below.
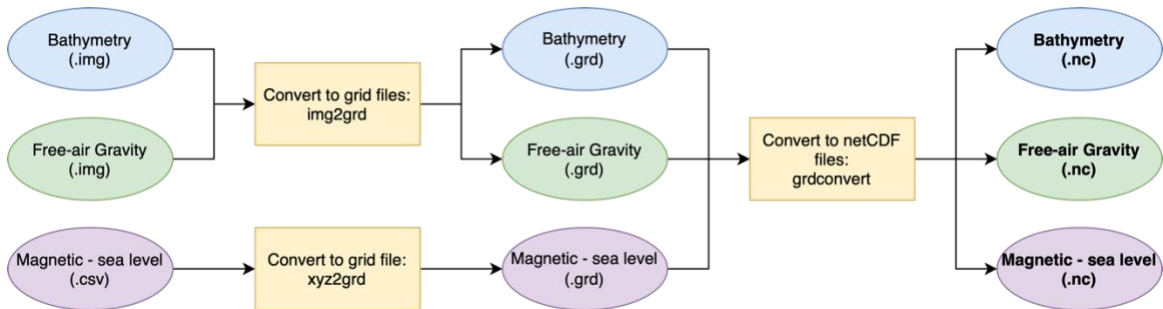
Figure 7: Conversion of data sets to grid files, and subsequently to netCDF files.

It should be noted that all data sets produced during this study were converted to netCDF files, the figure above only shows this process for the three initial data sets.

Initial Processing

Bathymetry – Directional Derivative

Like all derivatives, directional derivatives give us the rate of change of a function. Directional derivatives are taken when a function is a function of more than one variable, and thus there is more than one orientation in which one could take a derivative. The data sets used in this study can be thought of as functions of two variables: latitude and longitude. For example, bathymetry can be thought of as the function: $ocean\ depth(longitude, latitude) = f(longitude, latitude)$, where f is some function. Once we are thinking about our data sets as functions of two variables, we can take directional derivatives to explore how these data sets change along different paths (Alevizos, Greinert and Meysman, 2013). Let us think about taking a directional derivative from the North. Starting at the north edge of our data set, we "walk" southward, and record the slope of the data set at each point. Upward slopes are assigned positive values and downward slopes are assigned negative values.

The directional derivative of the bathymetry data was taken in order to produce a grid of false illumination. This is done by taking the directional derivative from the direction from which you wish to falsely illuminate, then normalizing the slope values using a cumulative Cauchy distribution. Resulting values of 1 are assigned the colour white, values of -1 are assigned black, and values in between complete the grey scale.
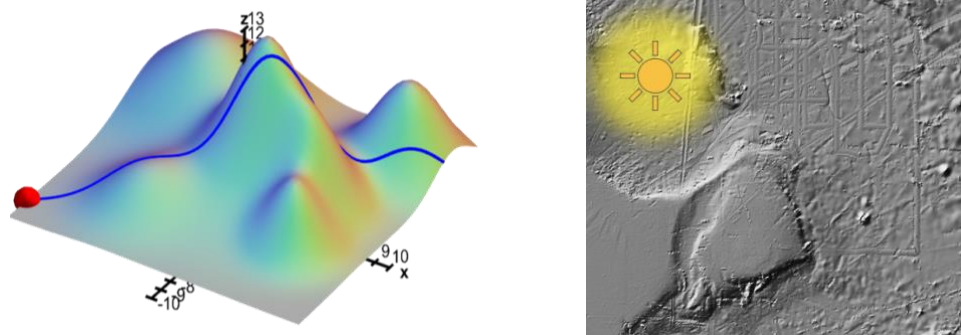
Figure 8: Illustration of walking along a function in one direction and recording the slope at each point (left); Example of directional derivative as false illumination (right).

The directional derivative of the bathymetry data was computed in GMT using the grdgradient function. The azimuthal direction chosen was -45° (NW), in order to illuminate both the N-S linear features (MAR) and the W-E linear features (CGFZ). The Nt1 flag was used for normalization and the process is outlined in the figure below.

Figure 9: Compute the directional derivative of the bathymetry data and convert to netCDF file.

Free-Air Gravity Anomaly – Bouguer Correction

The Bouguer correction was applied to the FAGA data set. This correction accounts for the density discrepancy between oceanic crust and sea water, which influences gravity measurements due to the effects of mass on gravitational field strength (Marchi, Ghidella and Tocho, 2014). The Bouguer correction was calculated in GMT using the gravfft function, computing up to the fourth power of bathymetry in the Parker expansion. The average difference between oceanic crust and sea water density was assumed to be 1665 kg/m^3 (Wessel et al., 2019). When subtracted from the free-air gravity anomalies, the bouguer anomaly is obtained. This process is outlined below.
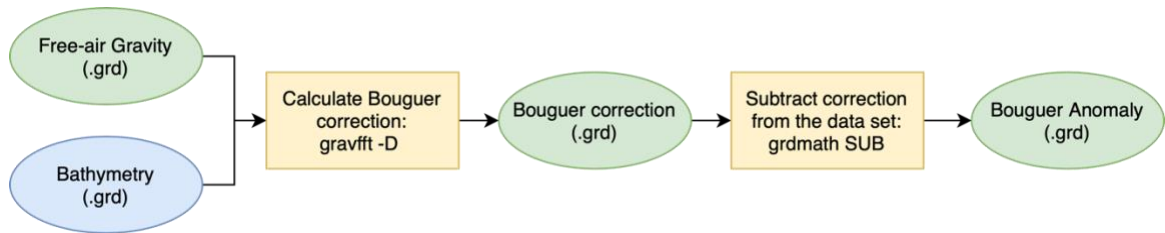
Figure 10: Calculation of the Bouguer anomaly from FAGA and bathymetry.

Magnetic Anomaly – Filling and Reduction to the Pole

During the initial plotting of the magnetic anomaly data set, several holes in the data set were observed. When compared to the maps of the data set provided by the NOAA – National Centres for Environmental Information, it was seen that these holes were a feature of the data set, and not an error in my reading or mapping processes. However, in order to perform a forward Fast Fourier Transform (grdfft) on this data set, the holes had to be filled in. This was accomplished using the function grdfill, with nearest neighbour interpolation. Since magnetic anomaly is a continuous field data set, a bilinear interpolation method would have been preferable to nearest neighbour. Unfortunately, this was not an option in GMT.

After the holes were filled, the reduction to the pole (RTP) anomaly was computed using the GMT function grdredpol. This is the anomaly that would be produced if all source bodies were magnetized vertically, and if the anomalies were observed at the geomagnetic pole. These two procedures are outlined below.

Figure 11: Procedure to fill NoData holes and compute the RTP anomaly from the MA data set.

Upward Continuation

Gravity and magnetic anomalies can be classified into two main groups: regionals and residuals. Regional anomalies are associated with broad features deep within the earth's interior. They are typically smooth, of large areal extent, and have high amplitudes. Residual anomalies, also referred to as local anomalies, are associated with smaller and more shallow features. They are of local areal extent and have lower amplitudes. Regional anomalies are long-wavelength (low frequency), while local anomalies are short-wavelength (high-frequency). Due to the fact that the regional

14

anomaly tends to be much larger in amplitude than the local anomaly, it is important that we have a way to effectively remove the regional anomaly from our data before attempting to interpret the data for local geologic structures (Ravat, 2007).

Upward continuation, with upward meaning away from the source of the field, is a method of smoothing data by attenuating the high frequencies. Reducing or removing high frequencies works to smooth the data since, as previously mentioned, high frequencies are associated with small, shallow, local anomalies. Very high frequencies are also often attributed to noise (Ravat, 2007). The smoothing effects of upward continuation can be observed in the figure below.
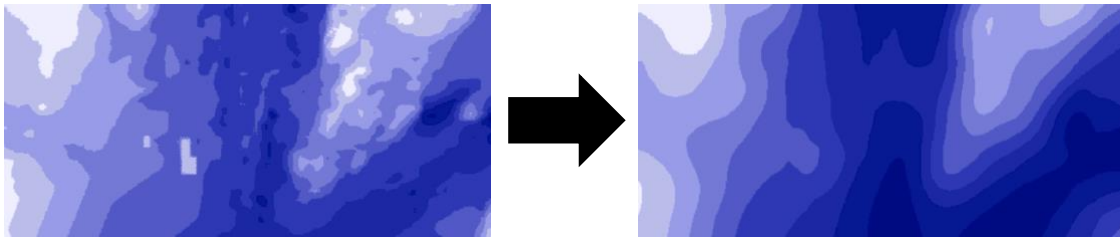
Figure 12: Illustration of the smoothing effects of upward continuation on a bathymetric data set (Adapted from DeLuca, 2022).

Upward continuation works to remove/reduce noise, suppress small-scale variation, and enhance regional trends. Thus, there was more to be done since our goal was to remove the regional trends and enhance the small-scale local anomalies. To achieve this goal, the upward continued data sets were subtracted from the original data set using grid math in GMT. This process was applied to both the FAGA and the MA-RTP data sets. One instance of this process is depicted in the figure below.
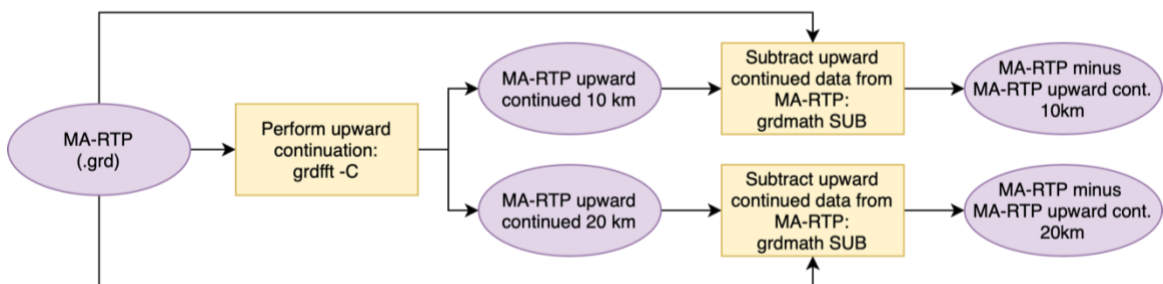
Figure 13: Process of removing regional trends from the magnetic anomaly data set (after filling and reduction to the pole) using upward continuation in GMT.

15

Wavelength Filtering and Directional Derivatives

Wavelength filtering is another technique with which we can isolate local anomalies. This process is slightly more selective and gives the user more choice over which frequencies they wish to enhance and which they wish to attenuate. The first step of wavelength filtering is to perform a Fourier Transform, which maps the data from the space domain into the frequency domain. This can be thought of as breaking up the complex signals into their component frequencies, as illustrated in the figure below.
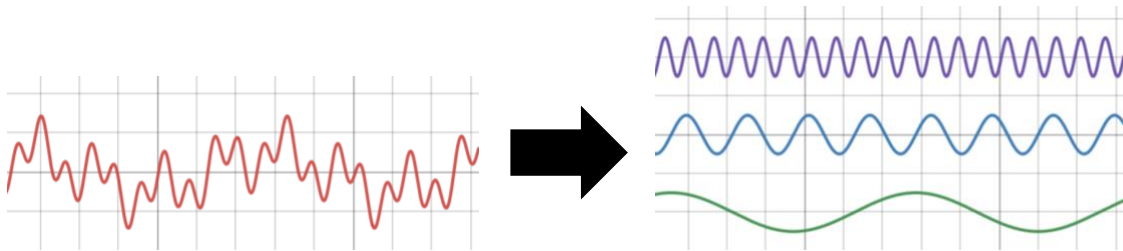
Figure 14: Decomposition of complex signal into its component frequencies.

Once the signal has been decomposed into its component frequencies, wavelength filters can be applied to filter out certain frequencies while allowing others to pass. There are three primary wavelength filters: high-pass, low-pass, and band-pass filters, which are named for the frequencies which they allow to pass.
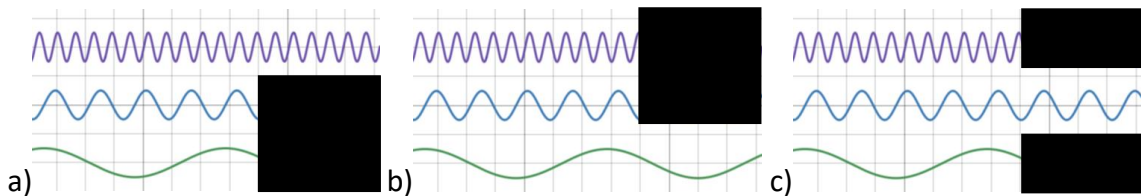
Figure 15: Illustration of a) high-pass filter, b) low-pass filter, and c) band-pass filter.

All three types of wavelength filters were applied to both the FAGA and MA-RTP data sets in GMT using the grdfft function. This function takes the 2D forward Fast Fourier Transform, applies a Gaussian filter using mathematical operations in the frequency domain, then transforms back to the space domain. Quite a bit of experimentation was required to determine the wavelength cut-off values for each filter. The final chosen wavelength values in meters are found in the table below.

Table 3: Wavelength values corresponding to the low/high cut-off frequencies of each filter.

Data Set:	High-pass Filter:	Low-pass Filter:	Band-pass Filter:
FAGA	50,000/-	-/90,000	85,000/55,000
MA-RTP	1,000/-	-/75,000	75,000/1,000

Directional derivatives of all filtered FAGA and MA-RTP data sets were then taken with the purpose of enhancing linear features. Taking a N-S directional derivative will enhance the appearance of W-E linear features, and similarly taking a W-E directional derivative will enhance the appearance of N-S linear features. Both N-S and W-E directional derivatives were taken, since the region of interest contains N-S linear features (the MAR) and W-E linear features (the CGFZ). See Table 2 above for a summary of all the data sets to which this was applied.

Creation of the Story Map

Before the story map could be made, all netCDF file data sets needed to be brought into ArcGIS Pro and made into raster files. This was done using the *Make NetCDF Raster Layer* tool in ArcGIS Pro. For the bathymetry data, I also applied the *Less Than* tool, to set any values greater than zero to zero, but maintain the value of any value less than zero. This was done so that all land masses, or other regions of elevation above sea level, would appear white on the maps, so that the coloured regions only represented regions below sea level. This complete process is outlined below.
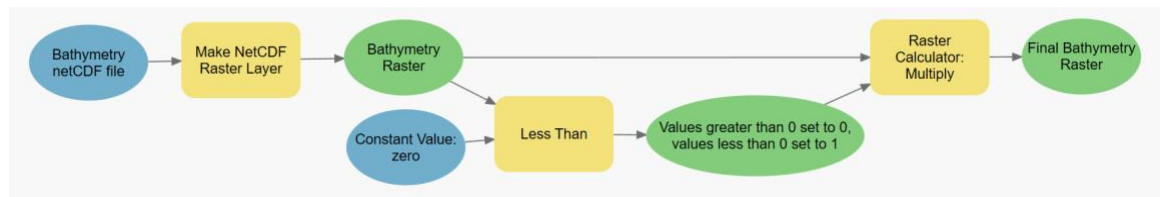
Figure 16: Procedure from bathymetry netCDF file to final raster layer in ArcGIS Pro.

Once each data set had been converted to a netCDF file, made into a raster layer in ArcGIS Pro, and published as a tile layer to ArcGIS Online, the story map was ready to be made. First, a WebMap was created for each set of data that was to be analyzed together. In the end there were four WebMaps made: one for an introduction to the project, study region, and bathymetry; one for the preliminary plotting and processing done to the FAGA and MA-RTP data; one for all upward continuation processing; and one for all wavelength filtering. This follows the same organization as this report. Once the four WebMaps were made, a Classic Tabbed Story Map was created to tie together the four WebMaps into one Story Map. Each WebMap was then accessible via the tabs at the top of the Classic Tabbed Story Map.

Results

Initial Plotting and Processing

Below are the results of plotting the bathymetry data set for the region of interest, and taking the directional derivative of this data set from the NW. The bathymetry map shows the shallow sloping sides of the MAR, as ocean depth decreases towards the peak of the ridge. It also displays the deep trenches of the two parallel fracture zones. The continental shelves of North America (bottom left) and Greenland (top left) can be seen with the highest elevations approaching 0 m above sea level. The normalized directional derivative plot succeeds in creating a sense of false illumination from the NW. The NW sides of elevated features appear illuminated, while the SE sides are in shadow.
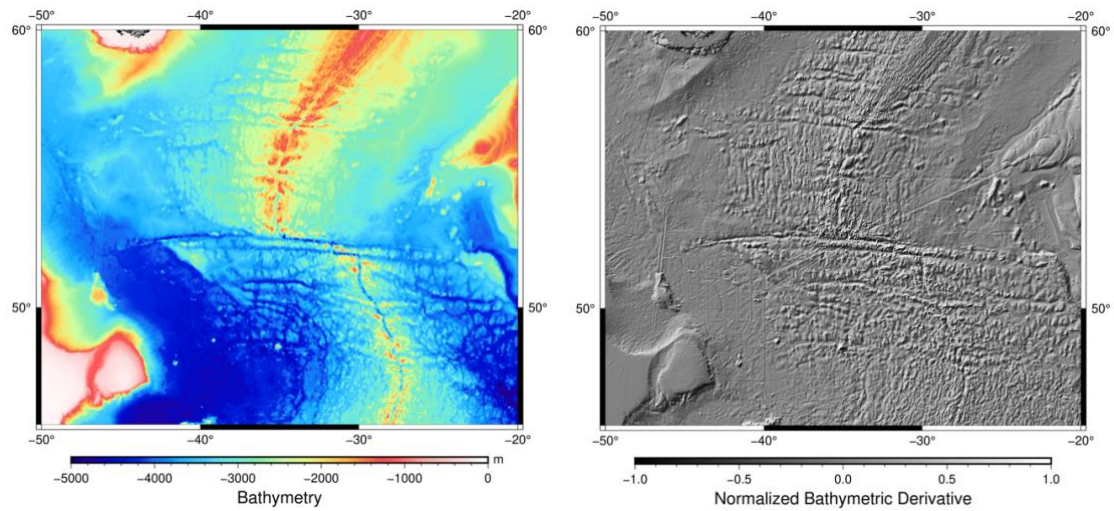
Figure 17: Bathymetry of the study region in meters above sea level (top). Normalized NW directional derivative of bathymetry (bottom).

The normalized directional derivative grid file was successfully used as an illumination source when plotting the other data sets. Applying this illumination source when plotting the bathymetry data results in the following figure. This provides a sense of texture to the plot and enhances viewers' understanding of the physical structure of the region.
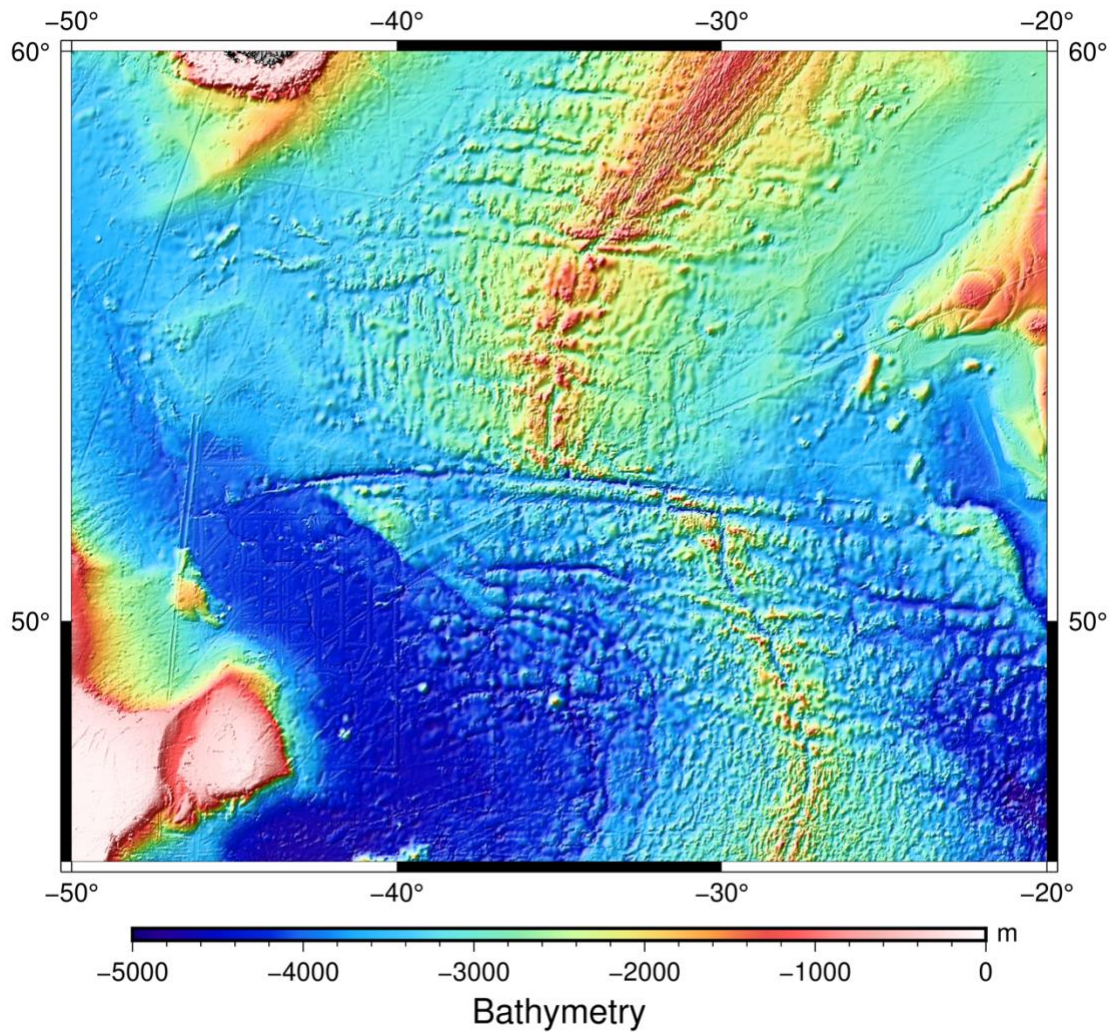
Figure 18: Combined image of bathymetry with illumination provided by the NW directional derivative.

The FAGA data was plotted both with and without the false illumination from the bathymetric derivative. While features that appear to be the MAR and CGFZ are both quite apparent without the illumination, adding illumination confirms that these linear features to in fact align with the MAR and the CGFZ. The Bouguer anomaly, derived from the FAGA, was also plotted both with and without illumination. Without illumination we see more of the small-scale details in the data through the use of the colour map, and with illumination we can again see how these anomalies align with the bathymetric landscape of the region.
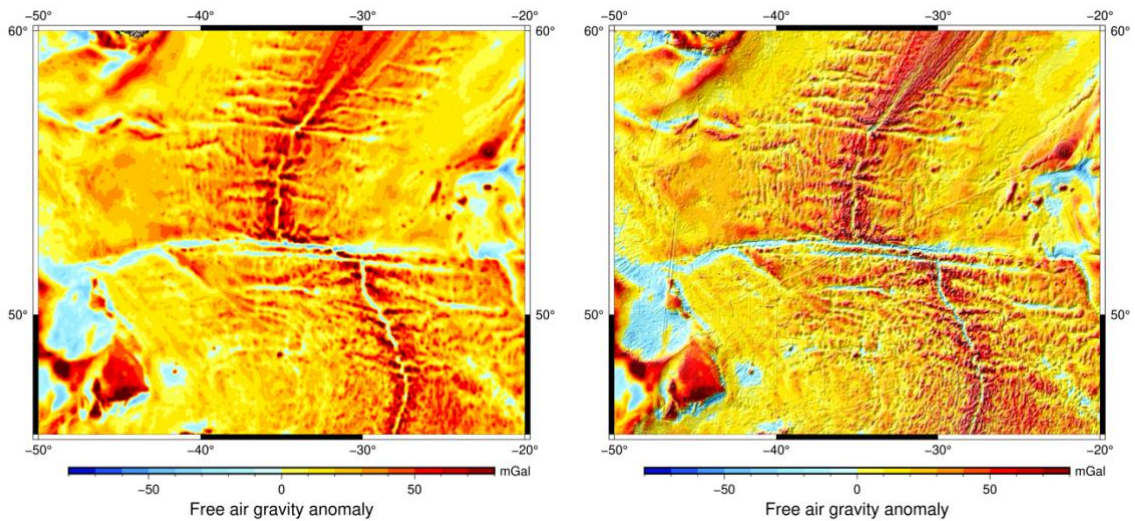
Figure 19: Free-air gravity anomaly without (left) and with (right) illumination from the NW directional derivative of bathymetry.
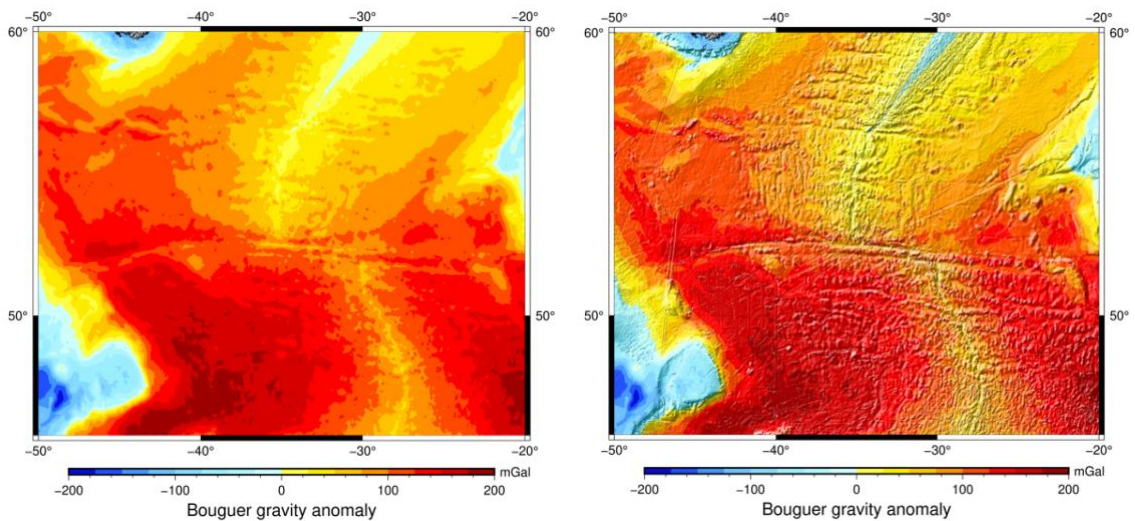
Figure 20: Bouguer gravity anomaly without (left) and with (right) illumination from the NW directional derivative of bathymetry.

The results of plotting the EMAG2v3 data set show that this region of the data set contains some holes (coloured in light grey). On this map it is not clear to see where the MAR and CGFZ lie, so it becomes extra useful to add the bathymetric illumination. Below, in Figure 22, are the resulting plots from filling the holes using nearest neighbour interpolation and computing the reduction to the pole anomaly.
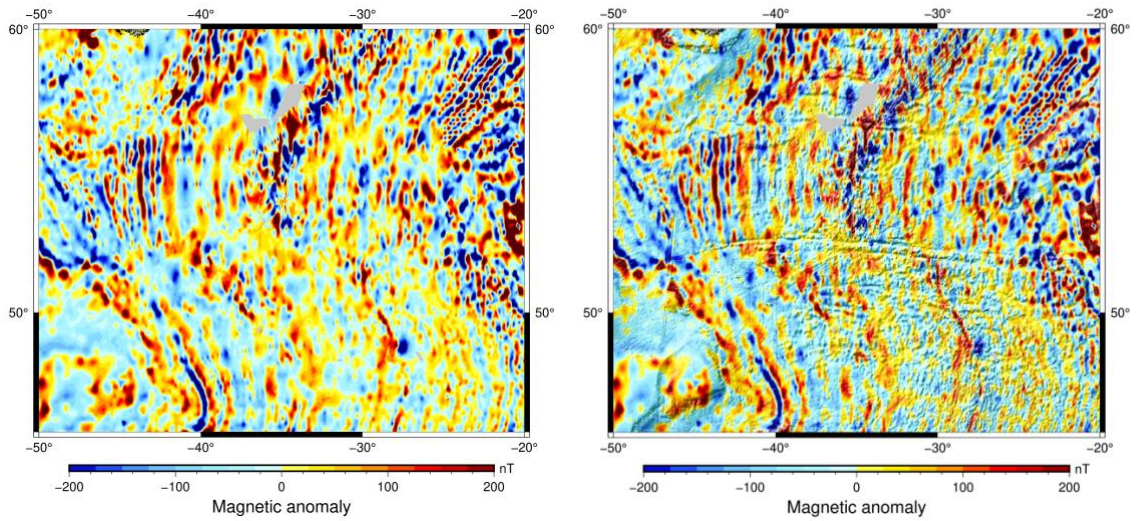
Figure 21: EMAG2v3 data set in study region without (left) and with (right) illumination from the NW directional derivative of bathymetry.
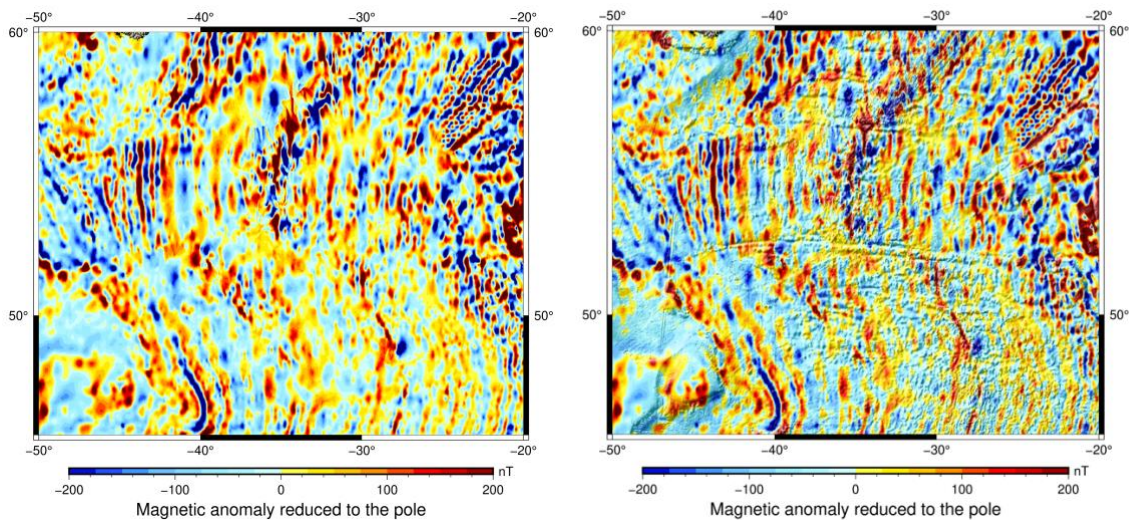
Figure 22: EMAG2v3 filled and reduced to the pole without (left) and with (right) illumination from the NW directional derivative of bathymetry.

Upward Continuation

The results of upward continuation can be seen in the figures below. The FAGA data was upward continued 10 km and 20 km – pictured on the top left and bottom left respectively. The upward continued data sets were then subtracted from the FAGA and those results are pictured on the top right and bottom right respectively. All data sets were plotted with illumination to overlay the bathymetric landscape onto the gravity anomaly data.
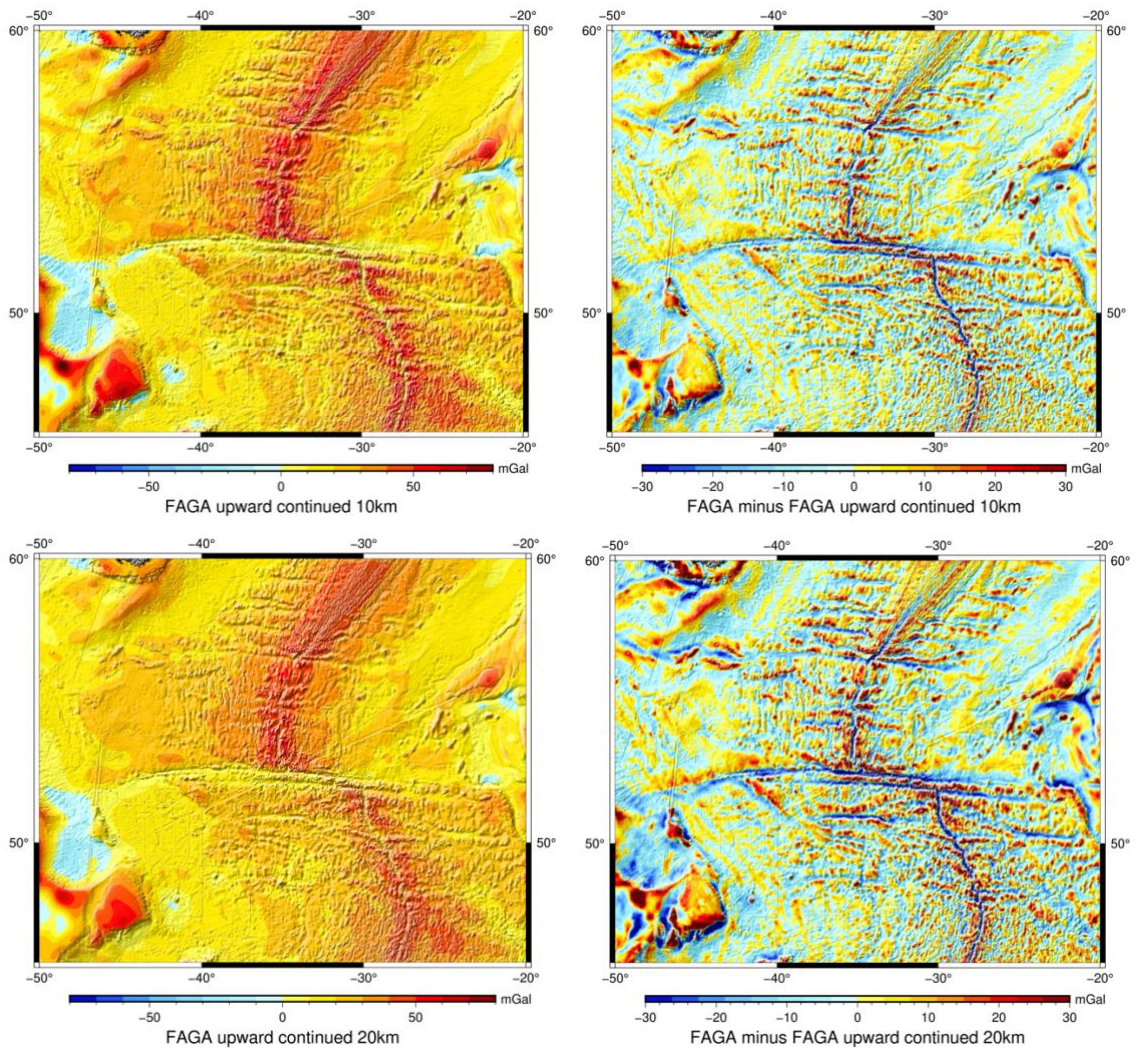
Figure 23: FAGA upward-continued 10 km and 20 km (top and bottom left); FAGA minus FAGA upward-continued 10 km and 20 km (top and bottom right).

The magnetic anomaly data filled and reduced to the pole (MA-RTP), was upward continued 10 km and 20 km – pictured on the top left and bottom left respectively. The upward continued data sets were then subtracted from the MA-RTP and those results are pictured on the top right and bottom right respectively. All data sets were plotted with illumination to overlay the bathymetric landscape onto the magnetic anomaly data.
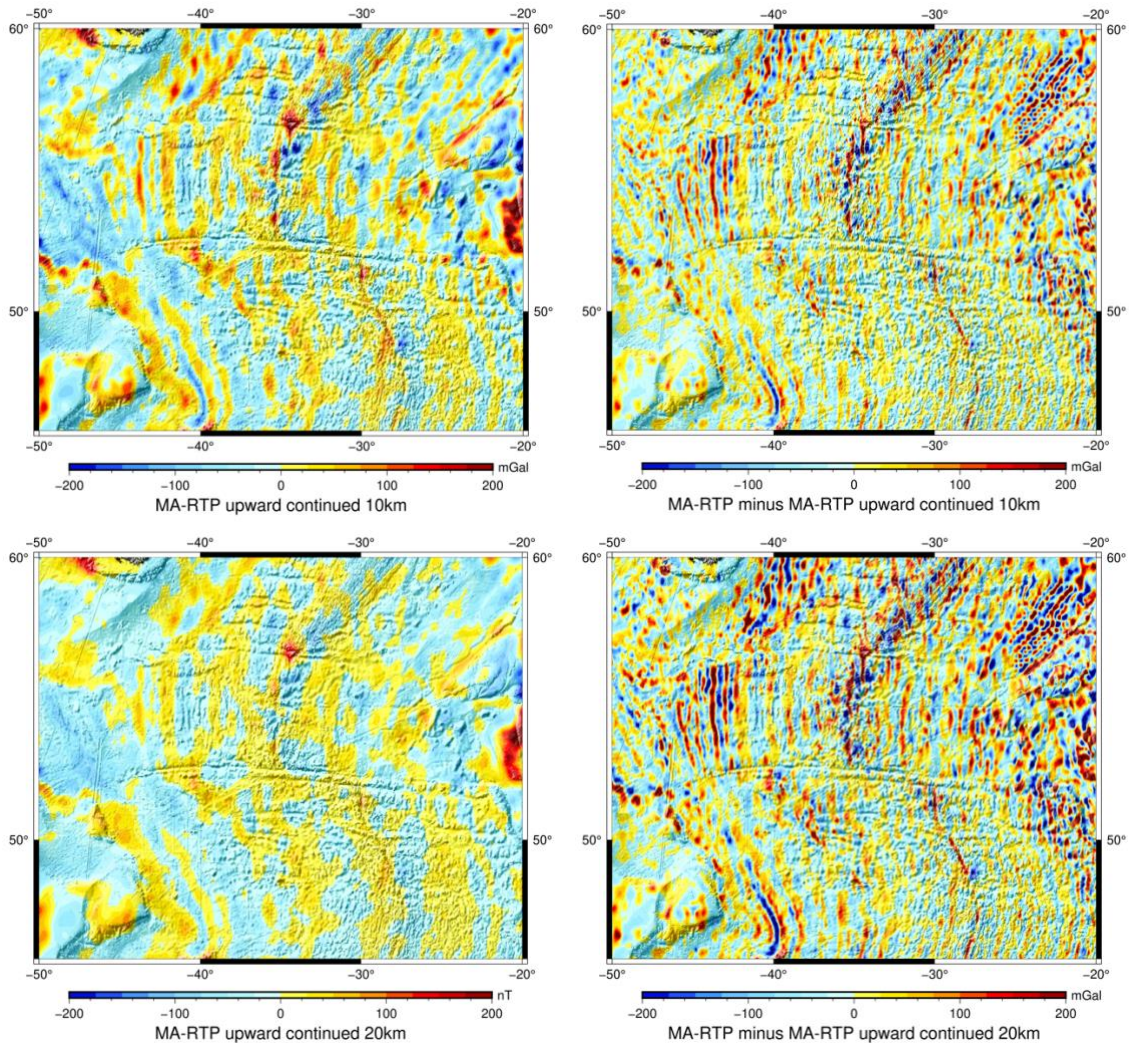
Figure 24: MA-RTP upward-continued 10 km and 20 km (top and bottom left); MA-RTP minus MA-RTP upward-continued 10 km and 20 km (top and bottom right).

Wavelength Filtering and Directional Derivatives

The following figures are all formatted as follows: filtered data on the left, normalized N-S directional derivative of the filtered data in the middle, and normalized W-E directional derivative of filtered data on the right.

The first three figures show the results from applying a high-pass, a low-pass, and a band-pass wavelength filter to the FAGA data, respectively.
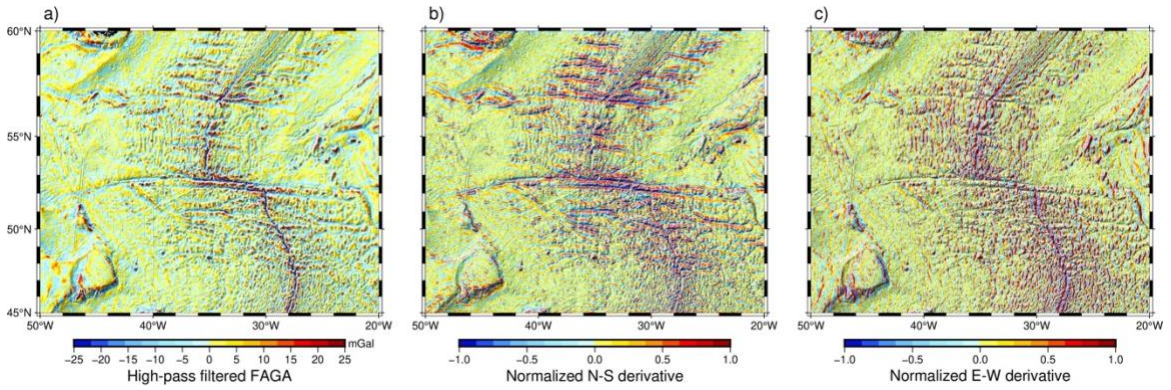
Figure 25: a) High-pass filtered FAGA; b) NS directional derivative of the high-pass filtered FAGA; EW directional derivative of the high-pass filtered FAGA.
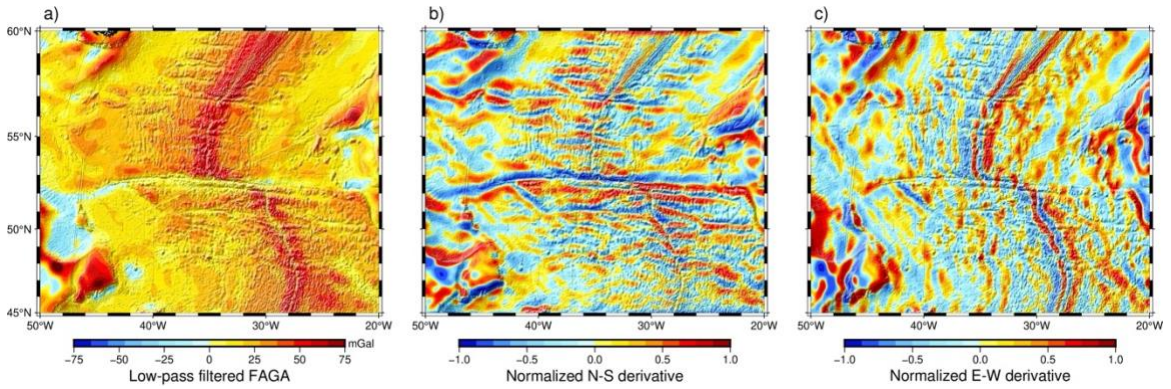
Figure 26: a) Low-pass filtered FAGA; b) NS directional derivative of the low-pass filtered FAGA; EW directional derivative of the low-pass filtered FAGA.
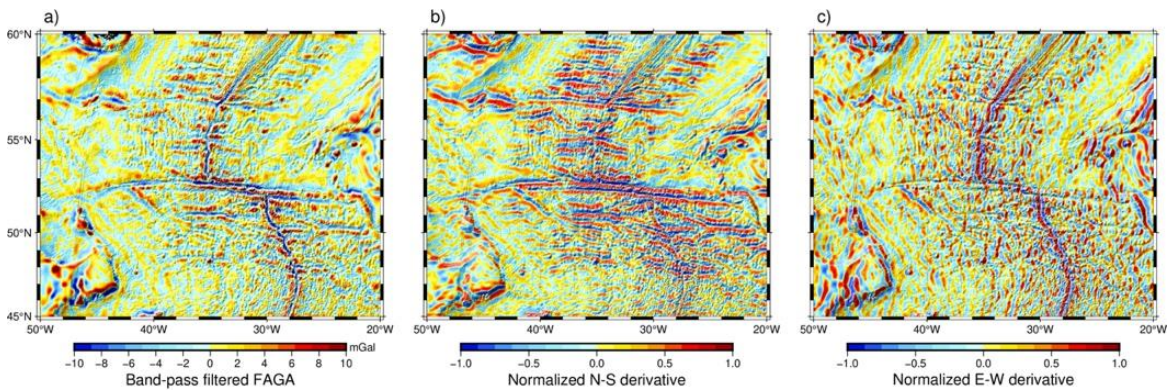
Figure 27: a) Band-pass filtered FAGA; b) NS directional derivative of the band-pass filtered FAGA; EW directional derivative of the band-pass filtered FAGA.

The next three figures show the results from applying a high-pass, a low-pass, and a band-pass wavelength filter to the MA-RTP data, respectively.
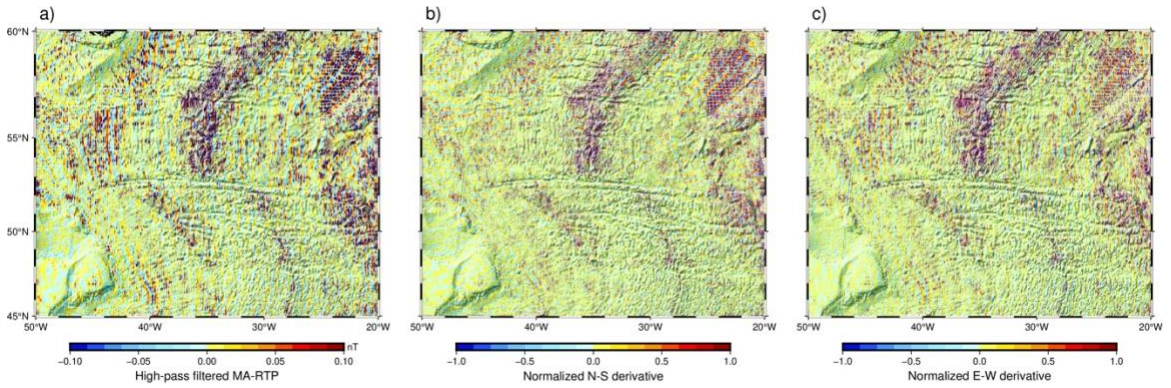
Figure 28: a) High-pass filtered MA-RTP; b) NS directional derivative of the high-pass filtered MA-RTP; EW directional derivative of the high-pass filtered MA-RTP.
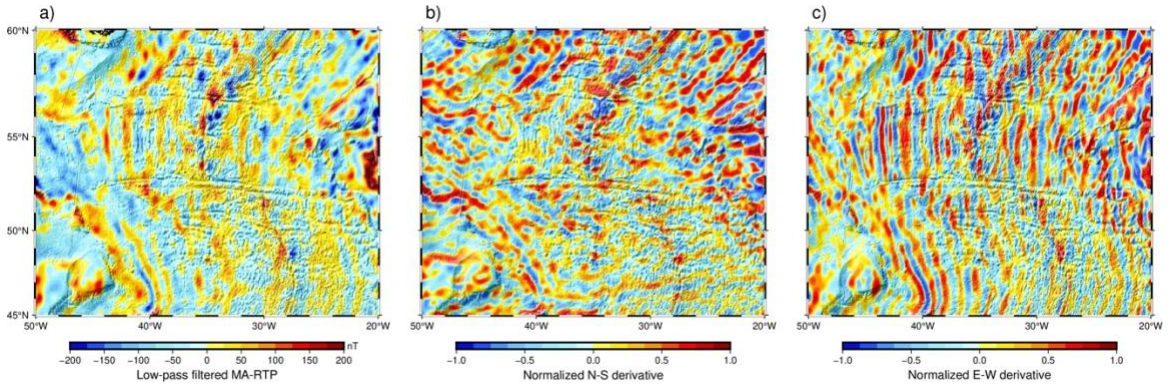
Figure 29: a) Low-pass filtered MA-RTP; b) NS directional derivative of the low-pass filtered MA-RTP; EW directional derivative of the low-pass filtered MA-RTP.
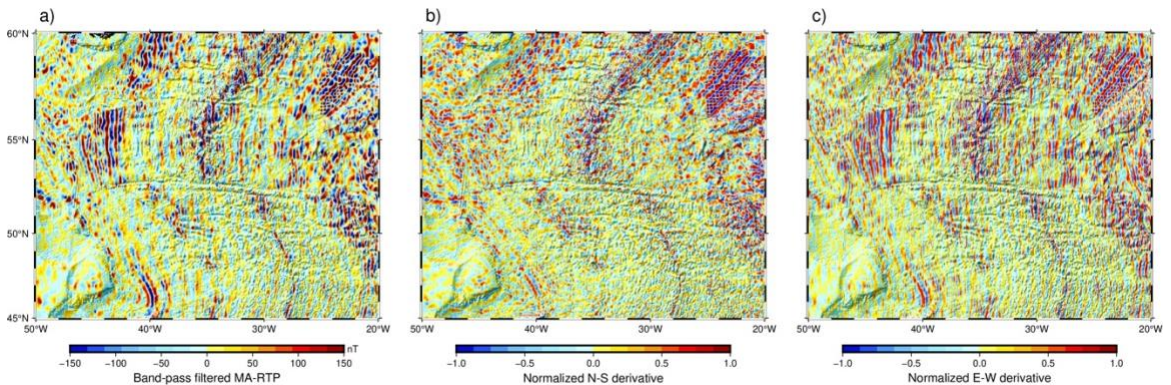
Figure 30: a) Band-pass filtered MA-RTP; b) NS directional derivative of the band-pass filtered MA-RTP; EW directional derivative of the band-pass filtered MA-RTP.

The Story Map

　　All maps included in each WebMap are interactive, meaning the user can zoom in or out, enter and exit map full-screen, and pan around the globe. This allows the user to explore according to their interests and choose how they wish to view the data. The WebMaps also make use of many useful features such as sidecar panels, the swipe feature, and vector pop-ups to display the information in a concise and engaging way. Below are examples of how these features were used on the introductory WebMap.
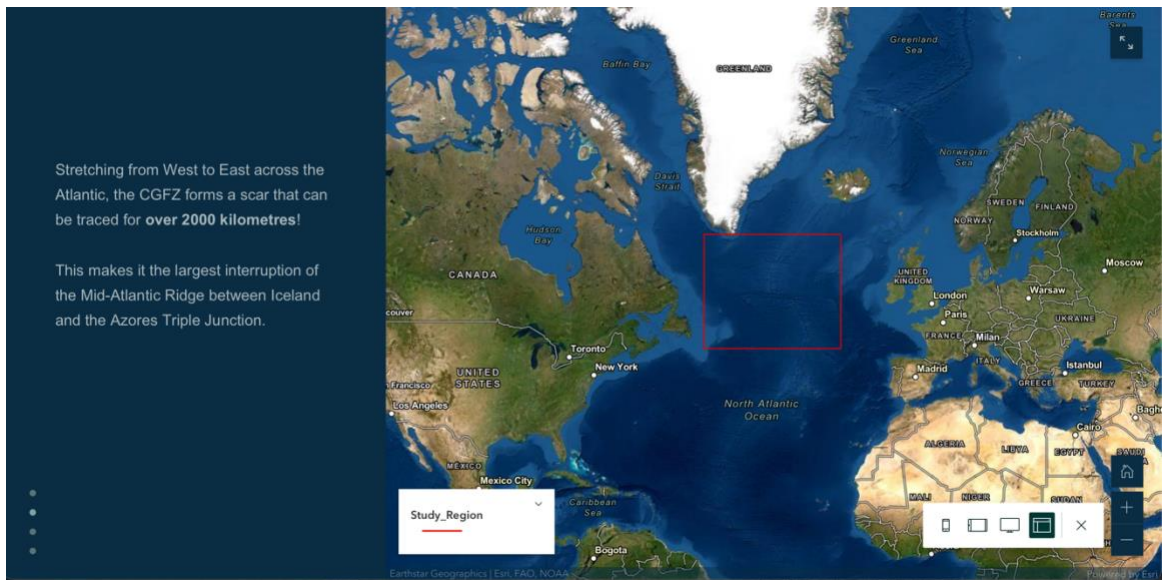
Figure 31: Screen capture of WebMap introducing the CGFZ. This sidecar panel automatically changes the map view on the right as the user scrolls through the information panels on the left.
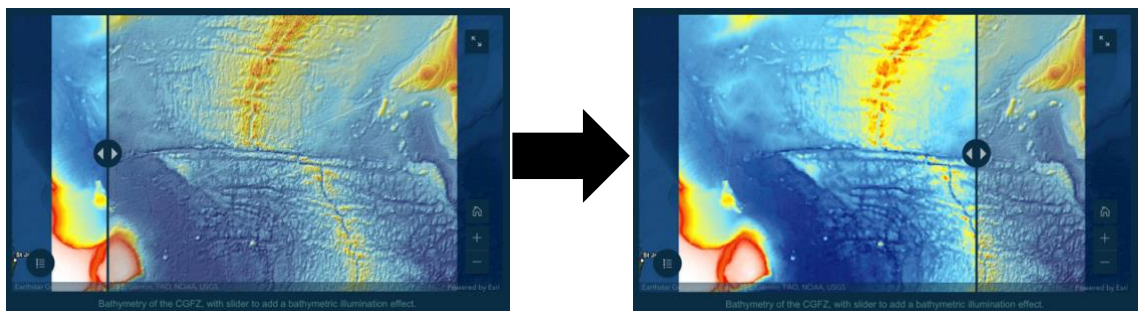
Figure 32: Screen captures of the swipe feature being used in the WebMap to add or remove the bathymetric illumination from the bathymetry data.
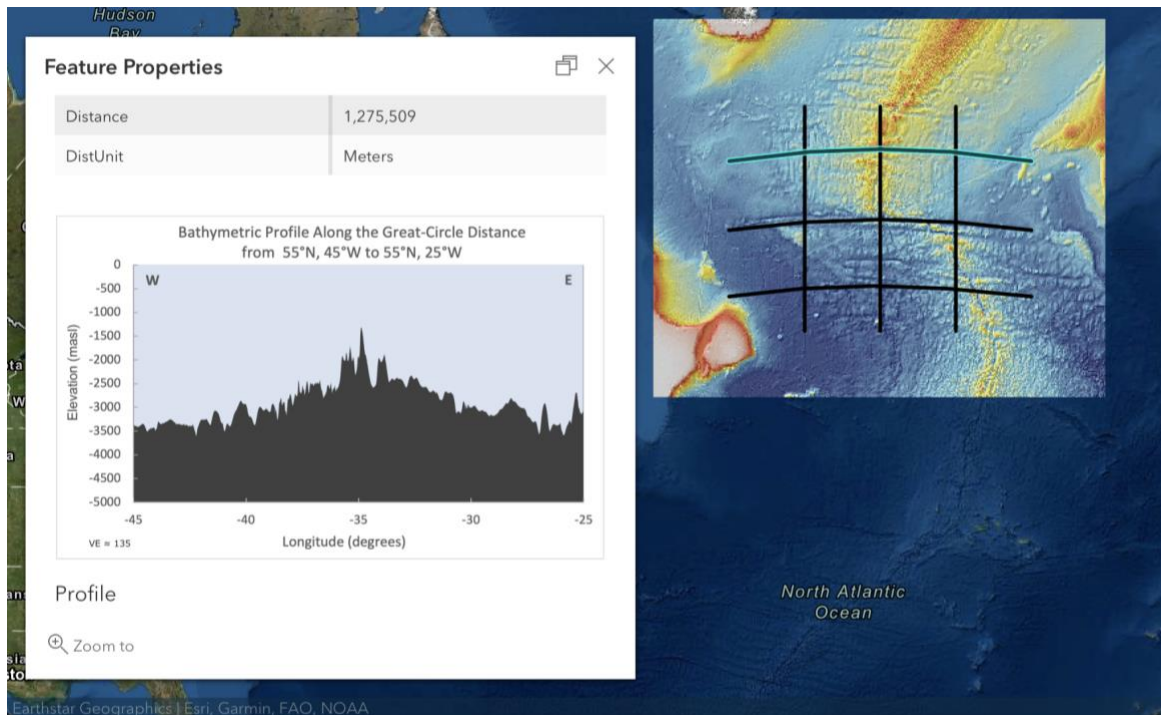
Figure 33: Screen capture of vector pop-ups in use on a WebMap. Here, the user can click on any transect on the map to view information regarding that transect including a vertical profile*.

*See Appendix for gravity and bathymetry profiles.

Discussion

Data Plotting and Processing

The bathymetry data reveals that the ocean south of the CGFZ is significantly deeper than north of the CGFZ. This could be due in part to differences in crustal composition, density, and rate of thermal subsidence. However, it is most likely due to differences in the processes occurring in the mantle that cause magma to rise to the surface, pushing the crust upwards and creating the ridge (Skolotnev et al., 2021a). It is predicted that Not only does the topography and ocean depth of this region have geological implications but also environmental and biological implications. The increase in elevation of the MAR is on the same order of magnitude as the Alps, and thus this gigantic feature greatly influences ocean currents, just as mountains such as the Alps influence air currents and weather. This range of differing ocean depths also increases the variety of ocean habitats and therefore increases the faunal and floral diversity of the region (Anon., 2022c).

Using the directional derivative of the bathymetry data set as the illumination grid when plotting another data set was a very useful procedure. This allows the viewer

to see the structure and topography of the terrain, without obscuring any of the colours that are representing values of another data set. The results of this process were verified by plotting the bathymetry data with the bathymetric derivative as illumination. The resulting plot (see Figure 18) was then observed to ensure that the areas of light and shadow align with the bathymetric values from the data set. Unsurprisingly, the two grids aligned perfectly, confirming that this illumination grid could be used on future maps. This method could be used for many applications where one data set is being analyzed and it would be useful to be able to see the "texture" of a secondary data set at the same time.

The free-air gravity anomaly map shows areas of strongest positive anomalies at the crest of the MAR, and at the tips of the three continental shelves visible in the study region. The majority of the entire region is positive anomalies, where the measured value of the gravitational field is stronger than the International Gravity Formula (IGF) predicts. One of the primary reasons for this is that this area on Earth is characterized by anomalous geoid highs, with an equipotential surface elevation approximately 40 m above the ellipsoid used for the calculation of the IGF (Hackney and Featherstone, 2003). The shallow ocean depths north of the CGFZ are abnormal when compared to other oceanic crust of the same age, and these large-scale properties are seen in no other intraplate or ridge centered volcanic province (Marquart and Schmeling, 2004). It is hypothesized that both this dynamic large-scale topography and positive gravity anomaly are due to an exceptionally warm mantle beneath the North-Atlantic and adjacent continental shelves (Marquart and Schmeling, 2004).

As we can see in Figure 19 when the bathymetric derivative is used to illuminate the FAGA data, regions of stronger positive anomalies align with regions of higher elevation while regions of weaker positive anomalies or negative anomalies align with regions of lower elevation. This is occurring because where the ocean is deeper, there is a larger mass deficiency below the measurement points. This makes the observed gravity value weaker than the theoretical value and generates a negative or weak positive anomaly. Where the ocean is shallower, such as at the crest of the ridge and over the continental shelves, there is less of a mass deficiency. There is therefore less of an effect on the measured versus theoretical gravity values, and we see strong positive anomalies due to the previously mentioned effects of the high geoid. Therefore the trends that can be seen in the FAGA maps are primarily influenced by the mass effects generated by the topography of the region.

To account for the effects of the seafloor topography, we can compute the Bouguer anomaly, plotted in Figure 20. This data set reveals trends in gravity anomalies that are almost exactly the reverse of what was observed in the FAGA. Here the negative and weakest positive anomalies are found along the crest of the MAR and over the continental shelves, while the strongest positive anomalies are found to increase with distance from the MAR. Now that the effects of bathymetry have been accounted for,

we are seeing the effects of the crustal and mantle densities. It is known that oceanic crust is the least dense where it is first formed along the crest of an MOR (Kearey, Klepeis and Vine, 2009). Here it is warm and less dense, then it becomes more and more dense as it cools and spreads away from the spreading center. The anomalies we see agree with this known trend of increasing crustal density with increasing distance from an MOR. Additionally, while the continental shelves had some of the strongest positive FAGA, they show negative Bouguer anomalies. I hypothesize that this is due to the fact that continental crust is significantly less dense than oceanic crust (Kearey, Klepeis and Vine, 2009). If the International Gravity Formula is using an average crustal density value, this would overestimate the density of the crust in these regions and result in the observed negative Bouguer anomalies.

In the magnetic anomaly map in Figures 21 & 22, the linear striations parallel to the spreading ridge of the MAR are apparent, even if they are somewhat obstructed by noise and small-scale anomalies. These N-S linear features alternate between positive and negative magnetic anomalies. This is due to the natural remanent magnetization (NRM), also known as paleomagnetism, of newly forming oceanic crust by the earth's magnetic field. As the plates pull apart and the new crust moves away from the spreading center, reversals in Earth's field are recorded and strips of alternating anomalies are generated running parallel to the MOR.

The holes that were filled in may not accurately represent the true anomaly values at those locations, however filling them was necessary to perform the forward Fast Fourier Transform. As previously mentioned, nearest neighbour interpolation is not ideal for continuous field data sets, and a more sophisticated method such as bilinear interpolation or cubic convolution could be used in the future if these areas were of specific importance. The computation of the reduction to the pole (RTP) does not appear to have made much difference to the data set. RTP removes anomaly asymmetry caused by inclination, as well as the effects of induced magnetisation and strike, so this may indicate that these effects were very small in this region (Zhang et al., 2018).

The upward continued FAGA data sets mapped in Figure 23 reveal the deep sourced anomalies and regional trends in the area. These trends were previously discussed, but are much more apparent and smooth after the upward continuation attenuated the noise and local anomalies. The upward continuation 20 km has been further smoothed than the upward continuation to 10 km, and thus is even more lacking in fine details and small scale features. After the upward continued data sets have been subtracted from the FAGA dataset, what remains are the small-scale local anomalies generated by shallower sources and some noise. In the resulting maps on the right we can see many apparent sources of local gravity anomalies, most roughly circular or linear in shape. One observation that was not evident on the FAGA map is that the gravity anomaly in the transform faults is a much stronger negative anomaly than the negative anomalies recorded in the associated fracture zones on either side. Many of these local

anomalies were not previously visible on the original FAGA map, and so this method has succeeded in isolating and enhancing small-scale anomalies.

With the MA-RTP data set, the smoothing effect of upward continuation didn't so much reveal a deep regional trend as it did simply smooth out extreme values towards the average. Because there is no clear regional trend, when these data sets were subtracted from the MA-RTP it resulted in very little new information. The resulting data sets, mapped in Figure 24, are very similar to the MA-RTP map. Therefore, this method was not as successful in isolating and enhancing small-scale magnetic anomalies.

In the high-pass filtered FAGA map, we see noise and some very shallow anomalies – features associated with high-frequencies. The N-S derivative was able to enhance some W-E linear striations in the filtered data set, primarily inside the FZ but also running perpendicular along the MAR segments both North and South of the CGFZ. The W-E derivative shows one main linear feature – a strong negative anomaly running N-S along the ridge valley of the MAR. In the low-pass filtered FAGA map, we see regional trends similar to the upward continued data – features associated with low-frequencies. The N-S derivative was able to enhance some W-E linear striations in the filtered data set, again primarily close to the FZ. The W-E derivative reveals a handful of alternating anomalies running N-S along the MAR. The band-pass filtered FAGA map was the most successful at selecting for features of interest while attenuating both noise and regional tends. The N-S derivative was able to enhance many W-E linear striations in the filtered data set, primarily inside the FZ but also running perpendicular across the MAR segments both North and South of the CGFZ. The W-E derivative shows a strong negative anomaly running N-S along the ridge valley of the MAR, and a few alternating stripes on either side.

In the high-pass filtered MA-RTP map, we see noise and some very shallow anomalies – features associated with high-frequencies. The N-S derivative was not able to reveal W-E linear features, which makes sense since we do not expect to see any in a magnetic anomaly data set so close to an MOR. The W-E derivative shows multiple N-S linear strips of alternating anomaly polarity. In the low-pass filtered MA-RTP map, we see a smoothed effect with a lack of clear regional trends similar to the upward continued data – features associated with low-frequencies. The N-S derivative did not reveal any W-E linear features. The W-E derivative reveals a handful of alternating anomalies running N-S along the MAR. Due to the smoothing effect of the feature, these striations do not accurately represent each magnetic pole reversal. The band-pass filtered MA-RTP map was again the most successful at selecting for features of interest while attenuating both noise and deeper anomalies. The N-S derivative revealed no W-E linear features. The W-E derivative shows several sets of alternating anomaly strips, the most evident being an area North-West of the CGFZ. The expected lineations running parallel to the MAR may not be evident in these results since the derivative was taken in a perfectly N-S orientation, while the MAR curves especially in the northern segment.

The Story Map

The tabbed story map has been successful in presenting the information from this study to members of the public in a new and educational way. While more complicated to produce, the tabbed story map aided greatly in delivering the information in an organized and comprehensible manner. By breaking up the contents into shorter sections each stored on a separate tab, the reader is less likely to become overwhelmed, confused, or lose interest. There is a lot of information and a many similar looking maps in this study, so prioritizing the clarity and conciseness of the story map was key.

Conclusions

GMT is an effective tool for the processing and plotting of various data sets. This software was used to investigate three geophysical properties of the Charlie-Gibbs Fracture Zone, the analysis of which can lead us to hypothesize and make new inquiries regarding the subsurface composition and structure of this region. Upward continuation was used successfully to isolate and enhance small-scale gravity anomalies for this region; however, it was not as successful in doing so for the magnetic data. Wavelength filtering allowed for the separation of signals based on desired frequencies, enabling us to attenuate noise and regional trends from the FAGA data. When paired with directional derivatives, this procedure led to the finding of both N-S and W-E linear features within the FAGA data set. The filtering was also successful on the MA-RTP data set, and directional derivatives confirmed the absence of W-E lineations but the presence of N-S lineations as was expected.

This final accumulation and presentation of the data using an ArcGIS story map shows that having a convenient medium in which to bring together, view, and compare previously disjointed data sets is highly beneficial for the dissemination of information. While all of the information stored in these data sets was previously only accessible to those who know how to code and process data using specific software, it can now be viewed by all.

References

Alevizos, E., Greinert, J. and Meysman, F.J., 2013. Using bathymetric derivatives to detect seabed features and assessment of backscatter variability of morphologically complex seabed. 2013, pp.OS33A-1757.

Anon. 2021a. *The Geological Society*. [online] Available at: <https://www.geolsoc.org.uk/Plate-Tectonics/Chap3-Plate-Margins/Divergent/Mid-Atlantic-Ridge> [Accessed 25 November 2021].

Anon. 2021b. *Understanding plate motions [This Dynamic Earth, USGS]*. [online] Available at: <https://pubs.usgs.gov/gip/dynamic/understanding.html> [Accessed 24 November 2021].

Anon. 2022c. *Mid Ocean Ridges across the planet | CHARLIE-GIBBS MARINE PROTECTED AREA*. [online] Available at: <http://www.charlie-gibbs.org/charlie/node/14> [Accessed 19 April 2022].

Bercovici, D., 2011. Mantle Convection. In: H.K. Gupta, ed. *Encyclopedia of Solid Earth Geophysics*. [online] Dordrecht: Springer Netherlands.pp.832–851. https://doi.org/10.1007/978-90-481-8702-7_130.

Cochran, J.R. and Talwani, M., 1978. Gravity anomalies, regional elevation, and the deep structure of the North Atlantic. *Journal of Geophysical Research*, 83, pp.4907–4924. https://doi.org/10.1029/JB083iB10p04907.

Coltice, N., Husson, L., Faccenna, C. and Arnould, M., n.d. What drives tectonic plates? *Science Advances*, 5(10), p.eaax4295. https://doi.org/10.1126/sciadv.aax4295.

Earle, S., 2015. 11.2 Earthquakes and Plate Tectonics. [online] Available at: <https://opentextbc.ca/geology/chapter/11-2-earthquakes-and-plate-tectonics/> [Accessed 17 April 2022].

Encyclopedia Britanica, Inc., 1994. *transform fault | geology | Britannica*. [online] Available at: <https://www.britannica.com/science/transform-fault> [Accessed 16 April 2022].

ESRI, 2022d. *2D, 3D & 4D GIS Mapping Software | ArcGIS Pro*. [online] Available at: <https://www.esri.com/en-us/arcgis/products/arcgis-pro/overview> [Accessed 18 April 2022].

Hackney, R.I. and Featherstone, W.E., 2003. Geodetic versus geophysical perspectives of the 'gravity anomaly'. *Geophysical Journal International*, 154(1), pp.35–43. https://doi.org/10.1046/j.1365-246X.2003.01941.x.

Hallam, A., 1971. Mesozoic Geology and the Opening of the North Atlantic. *The Journal of Geology*, 79(2), pp.129–157.

Hallam, A., 1975. Alfred Wegener and the Hypothesis of Continental Drift. *Scientific American*, 232(2), pp.88–97.

Hensen, C., Duarte, J.C., Vannucchi, P., Mazzini, A., Lever, M.A., Terrinha, P., Géli, L., Henry, P., Villinger, H., Morgan, J., Schmidt, M., Gutscher, M.-A., Bartolome, R., Tomonaga, Y., Polonia, A., Gràcia, E., Tinivella, U., Lupi, M., Çağatay, M.N., Elvert, M., Sakellariou, D., Matias, L., Kipfer, R., Karageorgis, A.P., Ruffine, L., Liebetrau, V., Pierre, C., Schmidt, C., Batista, L., Gasperini, L., Burwicz, E., Neres, M. and Nuzzo, M., 2019. Marine Transform Faults and Fracture Zones: A Joint Perspective Integrating Seismicity, Fluid Flow and Life. *Frontiers in Earth Science*, 7, p.39. https://doi.org/10.3389/feart.2019.00039.

Kearey, P., Klepeis, K.A. and Vine, F.J., 2009. *Global Tectonics*. Third ed. Wiley-Blackwell.

Keen, C.E., Dafoe, L.T. and Dickie, K., 2014. A volcanic province near the western termination of the Charlie-Gibbs Fracture Zone at the rifted margin, offshore northeast Newfoundland. *Tectonics*, 33(6), pp.1133–1153. https://doi.org/10.1002/2014TC003547.

Marchi, A.C.P.D., Ghidella, M.E. and Tocho, C.N., 2014. Analysis of Different Methodologies to Calculate Bouguer Gravity Anomalies in the Argentine Continental Margin. *Geosciences*, 4(2), pp.33–41.

Marquart, G. and Schmeling, H., 2004. A dynamic model for the Iceland Plume and the North Atlantic based on tomography and gravity data. *Geophysical Journal International*, 159(1), pp.40–52. https://doi.org/10.1111/j.1365-246X.2004.02398.x.

Meyer, B., Chulliat, A. and Saltus, R., 2017. Derivation and Error Analysis of the Earth Magnetic Anomaly Grid at 2 arc min Resolution Version 3 (EMAG2v3). *Geochemistry, Geophysics, Geosystems*, 18(12), pp.4522–4537. https://doi.org/10.1002/2017GC007280.

Molnar, P., 1988. Continental tectonics in the aftermath of plate tectonics. *Nature*, 335(6186), pp.131–137. https://doi.org/10.1038/335131a0.

Muller et al., 2019. Deforming plate reconstructions and associated digital supplements (Tectonics) – EarthByte. Available at: <https://www.earthbyte.org/muller-et-al-2019-deforming-plate-reconstruction-and-seafloor-age-grids-tectonics/> [Accessed 17 April 2022].

Pe-Piper, G., Piper, D.J.W., Jansa, L.F. and de Jonge, A., 2007. Early Cretaceous opening of the North Atlantic Ocean: implications of the petrology and tectonic setting of the Fogo Seamounts off the SW Grand Banks, Newfoundland. *The Geological Society of America Bulletin*, 119(5–6), p.712.

Pitman, W.C. and von Huene, R., 2020. Plate tectonics. *Access Science*. [online] https://doi.org/10.1036/1097-8542.527000.

Poldervaart, A., 1955. *Crust of the Earth: A Symposium*. Geological Society of America.

Ravat, D., 2007. Upward And Downward Continuation. pp.974–976. https://doi.org/10.1007/978-1-4020-4423-6_311.

Sæl, V.A.Z., Evolution, s vei 2A 0371 O.M.A.C. for E., PHONE, D. 1028 B.N.-0315 O.N. and CEED, E.-M. +47 22 85 40 97 C., 2021. *The secrets of marine transform faults - The Centre for Earth Evolution and Dynamics*. [online] Available at: <https://www.mn.uio.no/ceed/english/about/blog/2019/the-secrets-of-marine-transform-faults.html> [Accessed 3 October 2021].

Sandwell, D.T., Müller, R.D., Smith, W.H.F., Garcia, E. and Francis, R., 2014. New global marine gravity model from CryoSat-2 and Jason-1 reveals buried tectonic structure. *Science*, 346(6205), pp.65–67. https://doi.org/10.1126/science.1258213.

Skolotnev, S.G., Sanfilippo, A., Peyve, A.A., Nestola, Y., Sokolov, S.Yu., Petracchini, L., Dobrolybova, K.O., Basch, V., Pertsev, A.N., Ferrando, C., Ivanenko, A.N., Sani, C., Razumovskii, A.A., Muccini, F., Bich, A.S., Palmiotto, C., Brusilovsky, Y.V., Bonatti, E., Sholukhov, K.N., Cuffaro, M., Veklich, I.A., Ligi, M. and Dobrolybov, V.N., 2021a. Geological and Geophysical Studies of the Charlie Gibbs Fracture Zone (North Atlantic). *Doklady Earth Sciences*, 497(1), pp.191–194. https://doi.org/10.1134/S1028334X21030107.

Skolotnev, S.G., Sanfilippo, A., Peyve, A.A., Nestola, Y., Sokolov, S.Yu., Petracchini, L., Dobrolyubova, K.O., Basch, V., Pertsev, A.N., Ferrando, C., Ivanenko, A.N., Sani, C., Razumovskiy, A.A., Muccini, F., Bich, A.S., Palmiotto, C., Brusilovsky, Y.V., Bonatti, E., Sholukhov, K.N. and Cuffaro, M., 2021b. Seafloor Spreading and Tectonics at the Charlie Gibbs Transform System (52-53°n, Mid Atlantic Ridge): Preliminary Results from R/V a. N. Strakhov Expedition S50. *Ofioliti*, 46(1), pp.83–101.

Smith, W. and Sandwell, D., 1997. Global Sea Floor Topography from Satellite Altimetry and Ship Depth Soundings. *Science*, 277, pp.1956–1962.

Vogt, P., 2019. Mid-Oceanic Ridge. *Access Science*. [online] https://doi.org/10.1036/1097-8542.424750.

Wessel, P., Luis, J.F., Uieda, L., Scharroo, R., Wobbe, F., Smith, W.H.F. and Tian, D., 2019. The Generic Mapping Tools Version 6. *Geochemistry, Geophysics, Geosystems*, 20(11), pp.5556–5564. https://doi.org/10.1029/2019GC008515.

White, R.S. and Williams, C.A., 1986. Oceanic fracture zones. *Journal of the Geological Society*, 143(5), pp.737–741. https://doi.org/10.1144/gsjgs.143.5.0737.

Zhang, Q., Zhang, Y.T., Yin, G. and Li, Z.N., 2018. An improved frequency-domain algorithm for stable reduction to the pole at low latitudes. *Journal of Geophysics and Engineering*, 15(4), pp.1767–1782. https://doi.org/10.1088/1742-2140/aaa227.

Appendix – Gravity and Bathymetry Profiles

Gravity Anomaly and Bathymetry Profiles Along the Meridian 25°W

Gravity Anomaly and Bathymetry Profiles Along the Meridian 27°W

Gravity Anomaly and Bathymetry Profiles Along the Meridian 29°W

Gravity Anomaly and Bathymetry Profiles Along the Meridian 31°W

Gravity Anomaly and Bathymetry Profiles Along the Meridian 33°W

Gravity Anomaly and Bathymetry Profiles Along the Meridian 35°W

Gravity Anomaly and Bathymetry Profiles Along the Meridian 37°W

Gravity Anomaly and Bathymetry Profiles Along the Meridian 39°W

Gravity Anomaly and Bathymetry Profiles Along the Meridian 41°W

Gravity Anomaly and Bathymetry Profiles Along the Meridian 43°W

Gravity Anomaly and Bathymetry Profiles Along the Meridian 45°W

Average of the Eleven N-S Sampled Gravity Anomaly and Bathymetry Profiles